

UHECR Acceleration in Dark Matter Filaments of Cosmological Structure Formation

M. A. Malkov,^a R.Z. Sagdeev^b and P.H. Diamond^{a,c}

^aCASS and Department of Physics, University of California, San Diego, La Jolla, CA 92093-0424

^bUniversity of Maryland, College Park, MD 20742-3280

^cWCI Center for Fusion Theory, National Fusion Research Institute, Gwahangno 113, Yuseong-gu, Daejeon 305-333, Republic of Korea

E-mail: mmalkov@ucsd.edu

Abstract.

A mechanism for proton acceleration to $\sim 10^{21}eV$ is suggested. It may operate in accretion flows onto thin dark matter filaments of cosmic structure formation. The flow compresses the ambient magnetic field to strongly increase and align it with the filament. Particles begin the acceleration by $\mathbf{E} \times \mathbf{B}$ drifting with the accretion flow. The energy gain in the drift regime is limited by the conservation of the adiabatic invariant $p_{\perp}^2/B(r)$. Upon approaching the filament, the drift turns into the gyro-motion around the filament so that the particle moves parallel to the azimuthal electric field. In this 'betatron' regime the acceleration speeds up to rapidly reach the electrodynamic limit $cp_{max} = eBR$ for an accelerator with magnetic field B and the orbit radius R (Larmor radius). The periodic orbit becomes unstable and the particle slings out of the filament to the region of a weak (uncompressed) magnetic field, which terminates the acceleration.

To escape the filament, accelerated particles must have gyro-radii comparable with the filament radius. Therefore, the mechanism requires pre-acceleration that is likely to occur in structure formation shocks upstream or nearby the filament accretion flow. Previous studies identify such shocks as efficient proton accelerators to a firm upper limit $\sim 10^{19.5}eV$ placed by the catastrophic photo-pion losses. The present mechanism combines explosive energy gain in its final (betatron) phase with prompt particle release from the region of strong magnetic field. It is this combination that allows protons to overcome both the photo-pion and the synchrotron-Compton losses and therefore attain energy $\sim 10^{21}eV$. A customary requirement on accelerator power to reach a given E_{max} , which is placed by the accelerator energy dissipation $\propto E_{max}^2/Z_0$ due to the finite vacuum impedance Z_0 , is lifted by the cyclic operation of the accelerator.

Keywords: ultra high energy cosmic rays, acceleration of particles

ArXiv ePrint: [0000.0000](https://arxiv.org/abs/0000.0000)

Contents

1	Introduction	1
2	Accretion flow onto filaments and nodes in large scale structures	3
3	Particle acceleration around a filament	3
3.1	Details of particle motion	6
3.2	Final phase of acceleration	9
4	Energy losses and other energetic constraints	9
5	Summary and Outlook	12
A	Details of the flow and magnetic field structure	14
A.1	Dark matter gravitational potential	14
A.2	Plasma flow towards filament	16
A.3	Magnetic field around filaments and nodes	18
A.3.1	Magnetic Field around Nodes	18
A.3.2	Magnetic field around filament	19
B	Adiabatic invariant near separatrix	20

1 Introduction

A relatively strong, few μG galactic magnetic field precludes tracing Galactic cosmic rays (CR) back to their origins due to the magnetic orbit scrambling. Therefore, the long suspected link between CRs and supernova remnants (SNR) for example, even when convincingly established, will be indirect. The extra-galactic ultra-high energy CRs (UHECR), on the contrary, are open to what is called “astronomy with charged particles” (e.g., [1, 2]). Indeed, a 10^{20}eV proton has a 100 Mpc gyro-radius in a nano-Gauss intergalactic magnetic field. These particles propagate almost rectilinearly and may thus point back to the locations of the most sophisticated nature’s accelerators. From the theory side, however, there is as yet no astrophysical object which could be considered as an unquestionable candidate for acceleration and subsequent release of particles with such extreme energies.

An important recent progress in the emerging field of CR astronomy was made by the Auger team who were able to find the UHECR correlation with the large scale structure, as it traced by the AGN [3]. Some of the earlier studies also point at the UHECR clustering, e.g., [4], while other analyses incline towards a more isotropic distribution (see, e.g. [5, 6] for a review of the recent results and [7] for the updated Auger observations, downplaying to some extent the initial anisotropy finding). Notwithstanding the recent advances, the origin of the mysterious UHECRs remains unknown.

A necessary step for identifying the UHECR sources is to test the putative extragalactic accelerators for the capability to accelerate protons beyond 10^{20}eV . It seems natural to attempt at applying well advanced galactic CR acceleration mechanisms to such accelerators. The popular diffusive shock acceleration (DSA) is widely accepted as the most promising

mechanism to accelerate galactic CRs. Possible sites of its application to the UHECR acceleration are the cosmic structure formation shocks [8], gamma ray bursts [9–11] and the AGN environments [12, 13]. They have been examined in a number of publications, e.g., [13–17]. Remarkably, the DSA falls short by one order of magnitude to produce particles in the structure formation shocks with the highest energy observed, i.e. a few 10^{20} eV [14, 16], as the other scenarios encounter serious problems as well. At the same time, the DSA seems to be quite capable of accelerating particles to $\sim 10^{19.5}$ eV. However, while promising attempts to incorporate the CR-acceleration into simulations of the large-scale structure formation have been made [18–22], each of these two processes is scarcely feasible computationally, if all essential phenomena are included.

The purpose of this paper is to demonstrate that protons accelerated in the structure formation shocks to $\sim 10^{19.5}$ eV can be boosted to 10^{21} eV inside the same accretion flow. The suggested mechanism accelerates particles much faster than the DSA, thus sustaining against losses. It operates in plasmas accreting on to the gravitating dark matter (DM) filaments. Filaments, along with pancakes and knots are important elements of the cosmic structure formation which was established in a number of simulations (e.g., [19, 20, 23–26]) and seems to be supported observationally [27, 28]. The physical reason for the high acceleration rate of this mechanism can be readily understood by comparing it with the scatter-free shock surfing or shock drift acceleration mechanisms operating in perpendicular shocks [29–32]. Note, however, that the present mechanism does not require a shock in the flow, so a gradual flow compression suffices. When a rapidly gyrating high energy particle is slowly convected with the flow speed $u \ll c$ through a shock, the shock-particle interaction is adiabatic. The reason for that is a small $\sim u/c \ll 1$ momentum gain after each shock crossing and re-crossing. After $c/u \gg 1$ such cycles a particle of momentum p_{\perp} is left downstream with the net energy gain ~ 1 , or more precisely, to conserve the adiabatic invariant p_{\perp}^2/B , where B is the magnetic field (e.g., [33, 34]). The scatter-free mechanism works $\sim c/u \gg 1$ times faster than the DSA, since the upstream and downstream residence time is only of the order of gyro-period ω_c^{-1} , as opposed to the $c/u\omega_c$ idling time of the DSA. However, the duration of the scatter-free acceleration is too short to reach high energies. It should be noted that under certain circumstances its operation can be prolonged. For example, the cross shock potential can retain *nonrelativistic* particles at the shock against convection downstream.

In the mechanism proposed in this paper the role of retaining force plays the centrifugal potential that efficiently keeps particles against convection into the filament when the filament radius is sufficiently small. Initially, however, a particle is also convected by the flow towards the filament. As long as the particle drifts towards the center with the flow adiabatically, the magnetic moment p_{\perp}^2/B is conserved, and the particle gains energy according to this relation. At this phase of acceleration, the energy gain is relatively slow since the gyro-averaged work done by the azimuthal (motion) electric field approximately cancels out. However, if the particle has a gyro-radius $r_g \gtrsim R_f$ (filament radius), the particle adiabatic invariant strongly deviates from p_{\perp}^2/B before the particle sinks into the filament. Particle motion changes from the slow drift *towards* the filament to a nearly circular motion *around* it. The effect of work cancellation completely disappears and the particle enters into a betatron acceleration regime with a very fast (explosive) energy gain. Only after the orbit radius exceeds a critical value, the particle slings out of the filament vicinity. The acceleration rate drops since the motion electric field far away from the filament is weak and the acceleration virtually terminates.

The remainder of the paper is organized in two parts. The first, preparatory part deals with the configuration of accretion flow where the acceleration mechanism takes place, Sec.2

and Appendix A. Given the inability of the DSA to accelerate protons beyond 10^{20}eV , we focus on the principal possibility of acceleration to such extreme energies. Therefore, in the first part we limit our consideration to the most favorable for the acceleration, simple flow. The second part of the paper (Sec.3) deals with a detailed analytic description of the proposed acceleration mechanism. Ample numerical illustrations are also provided there. We estimate energy losses in Sec.4 and discuss other limitations of the mechanism in Sec5.

2 Accretion flow onto filaments and nodes in large scale structures

Before describing the particle acceleration mechanism in the cosmological structures, it is necessary to understand the geometry of magnetic and motion electric fields generated by the accreting plasma. A useful guidance is provided by numerical simulations performed within the ΛCDM model [24, 25, 35, 36, 37]. In such simulations, the gravitationally interacting dark matter (DM) particles aggregate to form a structure which then gravitationally drives conducting gas with the frozen in magnetic field. We will neglect the self-gravitation of the gas as it comprises only a relatively small fraction of the total mass. The emerging structures and thus the induced plasma flows are complicated in detail but morphologically generic. The matter accretes onto sheets, filaments and nodes and is thus organized in a “cosmic web” of massive nodes connected by relatively dense filaments along which the matter flows towards nearby nodes. The rest of the space can be considered as low density, low magnetic field “voids”.

Returning to the particle acceleration in such structures, we focus on a single filament with two nodes at its ends (a ‘dumbbell’), Fig.1. The dumbbell structure is supported by the DM accretion which is briefly discussed in A.1. To set up the acceleration scheme we note that the strong flow compression near the knots creates magnetic mirrors that confine energetic particles in the field-filament direction. A rarefied plasma accretes onto the filament from the surrounding void and stream then towards the nodes, while partially the plasma accretes onto the nodes directly from the void. The reaction from the magnetic field is negligible, so that we can split our task of setting out the magnetized flow configuration in the following two parts. First, we evaluate velocity and density distribution in the flow driven by the DM gravity, A.2. Second, we determine the magnetic field as being passively advected by the accreting gas from the ambient medium, A.3. According to the above consideration of the distribution of the magnetic and electric fields around a filament, it is not unreasonable to assume that, at least in the case of a favorable magnetic field orientation far away from the filament, the field is well aligned with the filament in the active acceleration zone. This assumption will be further discussed in Sec.5.

3 Particle acceleration around a filament

Based on the flow pattern discussed above, we consider a DM filament of radius R_f that accretes intergalactic gas in radial direction. We assume that the ambient magnetic field inside of an effective accretion volume (Bondi radius R_B) is aligned with the filament. We specify then \mathbf{B} as $\mathbf{B} = (0, 0, -B)$ with $B(r)$ depending only on $r = \sqrt{x^2 + y^2}$, the distance to the filament axis (z -axis), while particle motion in z -direction is constrained by magnetic mirrors near the filament end nodes. We do not include magnetic mirrors explicitly, but merely assume that the dynamics of accelerated particles is nearly perpendicular to \mathbf{B} , i.e.

$p_{\parallel} \ll p_{\perp} \approx p$. This assumption will be discussed in Sec.5. The equations of motion in the polar coordinates (r, ϑ) on the (x, y) plane read

$$\dot{p}_r = -\frac{p_{\vartheta}}{p} \left(eB - \frac{c}{r} p_{\vartheta} \right) \quad (3.1)$$

$$\dot{p}_{\vartheta} = \frac{p_r}{p} \left(eB - \frac{c}{r} p_{\vartheta} \right) + eE_{\vartheta} \quad (3.2)$$

$$\dot{r} = c \frac{p_r}{p} \quad (3.3)$$

$$\dot{\vartheta} = \frac{c}{r} \frac{p_{\vartheta}}{p} \quad (3.4)$$

where p_r and p_{ϑ} are the radial and azimuthal components of the particle momentum, $p = \sqrt{p_r^2 + p_{\vartheta}^2} \gg m_p c$ (with m_p being the proton rest mass), r is the particle radial coordinate, ϑ is the azimuthal angle, and E_{ϑ} is the azimuthal electric field. It is convenient to scale B to its value at infinity, $B_{\infty} = \text{const}$, both the radial coordinate r and the particle gyro-radius $r_g(p) = pc/eB_{\infty}$ to R_B (which is the Bondi radius, eq.[A.16]), and time, to R_B/c . Thus, the particle momentum p is now measured in the units of $eB_{\infty}R_B/c$. Since $E_{\vartheta} = -u_r(r)B(r)/c$, where $u_r < 0$ is the radial flow velocity, and since $ru_rB = \text{const}$, the motion electric field $E_{\vartheta} \propto 1/r$. It is thus suggestive to introduce the following parameter

$$v = -\frac{ru_rB}{R_BcB_{\infty}} > 0 \quad (3.5)$$

that controls both the drift of energetic particles towards the filament and their acceleration. Using these dimensionless variables (without relabeling), eqs.(3.1-3.4) rewrite

$$\dot{p}_r = -\frac{p_{\vartheta}}{p} \left(B - \frac{1}{r} p_{\vartheta} \right) \quad (3.6)$$

$$\dot{p}_{\vartheta} = \frac{p_r}{p} \left(B - \frac{1}{r} p_{\vartheta} \right) + \frac{v}{r} \quad (3.7)$$

$$\dot{r} = \frac{p_r}{p} \quad (3.8)$$

$$\dot{\vartheta} = \frac{1}{r} \frac{p_{\vartheta}}{p} \quad (3.9)$$

Note that due to the azimuthal symmetry, the angular variable ϑ is ignorable and only the first three equations need to be solved as a system. The angular variable ϑ is, however, useful in that it traces the particle energy. Indeed, by virtue of eqs.(3.6-3.7)

$$\dot{p} = \frac{vp_{\vartheta}}{rp}, \quad (3.10)$$

so that from eq.(3.9) we obtain

$$p - v\vartheta = \text{const}. \quad (3.11)$$

Furthermore, the azimuthal component of the particle canonical momentum

$$\mathcal{P}(t) = \Psi - rp_{\vartheta} \quad (3.12)$$

decreases linearly with time:

$$\mathcal{P} + vt = \text{const} \quad (3.13)$$

where $\Psi(r)$ is defined as follows

$$\Psi \equiv \int_0^r r B dr \quad (3.14)$$

Using eq.(3.12), it is convenient to reduce the dynamical system given by eqs.(3.6-3.8) to the following 1D Hamiltonian system

$$\dot{p}_r = -\frac{\partial p}{\partial r} \quad (3.15)$$

$$\dot{r} = \frac{\partial p}{\partial p_r} \quad (3.16)$$

where the particle momentum p assumes the role of the Hamiltonian

$$p(p_r, r, t) = \sqrt{p_r^2 + \left[\frac{\Psi(r) - \mathcal{P}(t)}{r} \right]^2} \quad (3.17)$$

Note that the time t enters the Hamiltonian through $\mathcal{P} = \mathcal{P}_0 - vt$. If $v = 0$, the relation $p = \text{const}$ provides a complete solution of the problem, at least in the form $t = t(r)$, seeing that $p_r = p\dot{r}$. We assume that $v \ll 1$, i.e. the plasma gravitational infall is slow compared to the speed of light. Therefore, we may consider both the change in the particle “total energy” p^2 and the deformation of the “potential energy” of the Hamiltonian in eq.(3.17) $U(r, t) \equiv (\Psi - \mathcal{P})^2 / r^2$ being adiabatic.

Given the above considerations, the particle dynamics is easily understood in terms of the critical points (i.e., points where $\partial U / \partial r = p_r = 0$) of the l.h.s. of eq.(3.15-3.16). One such point is where $\Psi(r) = \mathcal{P}$. It definitely exists for particles that move not too close to $r = 0$ with p being not too large. Specific conditions will be given below. Evidently, this particular critical point is the coordinate of the particle guiding center r_d , given by the following relation

$$\Psi(r_d) = \mathcal{P}_0 - vt. \quad (3.18)$$

Apart from drifting with the velocity $\dot{r}_d = -v/r_d B(r_d)$, particles oscillate in the potential well near its minimum, Fig.2. The following adiabatic invariant, which can be calculated using general principles of Hamiltonian dynamics, eqs.(3.15-3.17)

$$I = \oint p_r dr = \oint \sqrt{p^2 - U(r, t)} dr \simeq \pi p^2 / B(r_d), \quad (3.19)$$

is approximately conserved. The last relation in eq.(3.19) is valid in the guiding center approximation, discussed above. Since $\Psi \geq 0$ for all r , the solution of eq.(3.18) for r_d ceases to exist for $t > \mathcal{P}_0/v$. Formally this means that the particle guiding center reaches the origin, but the particle itself does not. Clearly, the guiding center approximation (gyro-phase averaged motion) breaks down before this moment and the full treatment of the dynamics (including the particle phase) is required. In particular, before the minimum of $U(r)$ at $r = r_d$ disappears, another minimum of U emerges at large $r = r_{\text{esc}} \gg r_d$. Here r_{esc} stands

for an 'escape' radius, since the particle makes a long excursion from the filament when it moves around this minimum of $U(r)$. In fact, it simply rotates in a weak magnetic field and has therefore a good chance to escape into the IGM. Naturally, a local maximum at $r = r_s$ appears between the two minima and a separatrix, which crosses the point $(r_s, 0)$, forms on the phase plane (r, p_r) , Fig.4 (see also Fig.3 for a numerical example of particle motion). These two additional critical points emerge at $t = t_c$ when

$$\frac{\partial^n}{\partial r^n} \left(\frac{\Psi(r) - \mathcal{P}(t_c)}{r} \right) = 0, \quad n = 1, 2$$

The critical time t_c and the radius r_c are therefore determined by the following relations:

$$\Psi''(r_c) = 0; \quad \mathcal{P}(t_c) = \Psi(r_c) - r_c \Psi'(r_c)$$

Starting from this moment, a particle, while still oscillating and climbing to higher energies in the left (narrow) potential well (see Fig.2) can also exercise finite motion in the shallow right potential well, provided that particle energy is high enough. The moment $t = t_s$, and the particle momentum p_s when the particle moves from the left to the right potential well, can be determined from the following relations

$$\mathcal{P}_s = \Psi(r_s) - r_s \Psi'(r_s); \quad \Psi'(r_s) = p_s$$

where $\mathcal{P}_s = \mathcal{P}_0 - vt_s$. These are two equations for the three unknowns (p_s, r_s and \mathcal{P}_s) and the conservation of adiabatic invariant may be used as the third equation. However, when the particle orbit approaches the separatrix, the simplified drift theory approximation in eq.(3.19) becomes inaccurate. This is illustrated in Figs.5 and 6. The integral representation of the adiabatic invariant will be used below for the treatment of this final phase. Note that this is the most efficient phase of the acceleration mechanism. What happens is that particles, while dwelling progressively longer at the hyperbolic point during their oscillations in the potential well, virtually circulate around the origin, being thus in a 'betatron' acceleration regime. The energy gain is very fast (explosive, as we shall see) at this stage, since the electric field of the accreting plasma is almost collinear to the particle velocity. At the same time the orbit radius decreases since the magnetic field increases fast enough along the particle orbit.

3.1 Details of particle motion

To describe further details of the particle dynamics, we specify the magnetic field profile $B(r)$. Since it is essentially identical to the density profile (see the end of A.2) we can utilize the expression in eq.(A.14). For convenience, we slightly modify it by representing $B(r)$ (in dimensionless variables) as

$$B(r) = r^{-\nu} + 1 \tag{3.20}$$

with $\nu = 1/(\gamma - 1)$. The difference between the last expression and the corresponding density profile is insignificant, given the approximate character of eq.(A.14). This approximation is acceptable as it ensures the field compression that is equivalent to the density compression when r changes from $r \gtrsim 1$ to $r \ll 1$.

We may now explicitly identify the separatrix parameters

$$\mathcal{P}_s \simeq \frac{\nu - 1}{2 - \nu} p_s^{-(2 - \nu)/(\nu - 1)} \quad \text{and} \quad p_s = r_s + r_s^{1 - \nu} \simeq r_s^{1 - \nu}, \tag{3.21}$$

that relate the particle momentum p_s , its orbit radius r_s and the canonical momentum \mathcal{P}_s (or, equivalently, the time t_s) at the moment of separatrix crossing. To simplify the calculation of the adiabatic invariant I in eq.(3.19), we set the gas adiabatic index $\gamma = 5/3$, i.e. $\nu = 3/2$ in eq.(3.20). For now, it is sufficient to evaluate the adiabatic invariant at the moment of separatrix crossing, that means the moment when a particle goes from the left potential well to the right one in Fig.2, that is

$$I_s \equiv I(p_s) \approx 2 \int_{r_{s,\min}}^{r_s} \sqrt{p_s^2 - \left(\frac{2\sqrt{r} - \mathcal{P}_s}{r}\right)^2} dr \quad (3.22)$$

where $r_s \approx 1/p_s^2$, $\mathcal{P}_s = 1/p_s$, and $r_{s,\min} = (\sqrt{2} - 1)^2 / p_s^2$. A simple integration yields

$$I_s = \frac{2}{p_s} \left(4 \ln \frac{1}{\sqrt{2} - 1} - \pi \right) \quad (3.23)$$

From the conservation of adiabatic invariant we thus have

$$I_0 = \pi \frac{p_0^2}{B_0} = I_s \approx \frac{0.77}{p_s} \quad (3.24)$$

where p_0 and B_0 are the particle momentum and the magnitude of the magnetic field at a certain point in the flow far away from the filament (where the drift approximation still applies). If a particle of the momentum p_0 enters the acceleration process at $r_0 \gg R_B$, then $B_0 = 1$. To include particles injected closer to the filament axis, e.g. from a shock in the accretion flow that diffusively preaccelerates particles, we retain the term with $B_0 > 1$. Such particles may be injected from one of the nearby nodes (clusters) where strong shocks are expected to diffusively accelerate cosmic rays with high efficiency, e.g., [8, 18, 20–22, 38].

From the last equation we obtain the following interesting (inverse-square) relation between the initial and the final (separatrix value) particle momentum

$$p_s \approx 0.25 \frac{B_0}{p_0^2} \quad (3.25)$$

Fig.7 shows the results of numerical integration of a few particle orbits along with the curves corresponding to eq.(3.25). Noticeable deviations are seen only at unrealistically high values of p_s , which are quite understandable, though (see Sec.3.2 below and the discussion in Sec.5).

However, this seemingly strong energy gain should be taken with care. Since $p_s \approx 1/\sqrt{r_s}$, the maximum momentum p_s is limited by the condition $r_s \gtrsim r_t$, where $r_t \ll 1$ is the radius below which the flow changes its direction from radial (towards filament) to axial (towards node). Particles with sufficiently small gyro-radii are convected along the z -axis out of the acceleration zone. This constitutes the re-acceleration character of the process and constrains the initial particle momentum p_0 . In order to reach the separatrix and escape the accelerator *before* being convected towards one of its end nodes, a particle must enter the acceleration with the momentum

$$p_0 > \sqrt{0.25 B_0 r_t^{1/4}} \quad (3.26)$$

This is a significant but not the prohibiting constraint on the initial particle momentum. The final particle momentum p_{\max} is limited by the condition $p_{\max} \leq \min(r_t^{-1/2}, p_s)$. If

$p_s > r_t^{-1/2}$, the particle cannot be released from the accelerator and sinks into the filament. The illustration of the above consideration is given in Fig.8.

As a proxy for r_t , an estimate of magnetic field and/or density compression between the flow outside of the accretion radius and the filament axis can be used. So, a $\sim 10^3$ increase in B from the nanogauss IGM field to the μG intracluster field appears to be reasonable. With the $r^{-3/2}$ scaling of the magnetic field adopted above, this translates into $r_t \sim 10^{-2}$, yielding, in turn, $p_{\text{max}} \sim 10$ for $p_0^2 \sim 1/10$. Therefore, if a particle enters the acceleration at a few 10^{19}eV it may reach 10^{21}eV by the moment of ejection.

Nevertheless, it is worth while to return to the dimensional variables and recall that the length (including the Larmor radius) is measured in the accretion radii R_B , eq.(A.16), that can be approximated as

$$R_B \approx 2.1 \frac{M_f}{10^{13} M_\odot} \frac{10^6 K}{T_\infty} \text{Mpc}, \quad (3.27)$$

where T_∞ is the IGM temperature (i.e. well outside the accretion radius). Thus, the maximum particle energy can be represented as follows

$$E_{\text{max}} \approx 2 \cdot \min \left\{ 0.25 \frac{B_0}{B_\infty} \left(\frac{R_B}{r_{g0}} \right)^2, \sqrt{\frac{R_B}{r_t}} \right\} \frac{M_f}{10^{13} M_\odot} \frac{10^6 K}{T_\infty} \frac{B_\infty}{\text{nG}} \text{EeV} \quad (3.28)$$

The major uncertainty is the accretion radius, eq.(3.27), to which the Larmor radius and thus the maximum energy are scaled. We note here in passing, that the accretion radius has a somewhat ambiguous relation to the accretion rate $\dot{M} = 4\pi \lim_{r \rightarrow \infty} r^2 u_r(r) \rho(r)$, as it formally involves a limiting transition if this radius is to be determined from the ambient density and temperature. Indeed, while the density has a definite limit ρ_∞ , the other two comprise a $0 \cdot \infty$ -type uncertainty, so one is left with a sonic radius to accept as an accretion radius R_B . At the same time, if R_B is not much larger than l , the form of the surface from which the gas effectively accretes onto the filament-node 'dumbbell' structure is more complicated than a sphere, Sec.A.2.

Assuming, however, $R_B > 2l$, let us attempt to estimate the absolute value of R_B and thus E_{max} in the above expressions. According to the simulations of the large scale structure formation, the gas temperature inside the filament is expected to be in the range $10^5 - 10^7\text{K}$, e.g., [24, 37, 39]. These predictions seem to be confirmed by recent observations of Abell 222/223 clusters of galaxies [40]. However, a lower temperature may be appropriate for eq.(3.27) as it refers to the outskirts of the accretor, Sec.A.2. In addition, there are also observations of filaments with significantly lower temperatures [27], $T \lesssim 10^5\text{K}$ or even $T \ll 10^5\text{K}$, where the latter case, however, is rather an indication of the presence of cold clouds. The mass of the Abell 222/223 filament [40] is found to be $M_f \simeq 10^{14} M_\odot$ and its length $2l \simeq 15\text{Mpc}$. These figures translate into R_B in eq.(3.27) that can formally reach 100Mpc (for $T_\infty = 2 \cdot 10^5\text{K}$) and beyond, which would be enough to reach 10^{21}eV for $B_\infty \simeq 1\text{nG}$ and $\sqrt{R_B/r_t} \simeq 10$ (see Sec.A.2). In addition, the filament end nodes may also effectively increase M_f thus enhancing R_B and E_{max} and compensating for possibly higher T_∞ . Note that r_t is then of the order of 1 Mpc (based on its simple estimates in Sec.A.2 from the three orders of magnitude density and magnetic field compression in the accreting flow) while the initial particle gyro-radius should be of the order of 10Mpc.

While the observations of the cosmic web filaments are important for the proposed acceleration mechanism, the latter is yet to be elaborated to the level of a predictive model in

which the observational parameters may be fully used. Clearly, the size of the axial stream r_t remains to be consistently determined from at least two-dimensional hydrodynamic treatment beyond the simplified approach in Sec.A.2. We note that such treatment may reduce r_t thus improving the acceleration, particularly if the gas cooling is taken into account, e.g.,[41]. We will discuss other kinematic limitations of the acceleration in Sec.5.

3.2 Final phase of acceleration

To complete our description of the proposed acceleration mechanism, here we consider its final stage in some detail. This is the most important phase of the acceleration since the energy losses, which will be briefly addressed in the next section, become progressively important with growing energy and may terminate the acceleration before the required energy is reached.

As we showed in the previous section, the maximum momentum (more precisely the momentum at the instant of separatrix crossing) may be determined from the conservation of the particle adiabatic invariant. The particle trajectory, including its part immediately preceding the separatrix crossing, can be described by this principle as well. In particular, the time dependence of the particle momentum short before the separatrix crossing can be written as follows (see Appendix B)

$$p(t) = \frac{1}{\mathcal{P}_0 - vt} \quad (3.29)$$

The acceleration time (conventionally defined) thus reduces towards the end of acceleration

$$\tau_a = \frac{p}{\dot{p}} = \frac{1}{\nu p} \quad (3.30)$$

which is in sharp contrast with the DSA, for example, where the acceleration time grows linearly with p (at least for Bohm diffusion). The acceleration termination time (separatrix crossing) is somewhat uncertain, because the separatrix itself is determined for a fixed value of \mathcal{P} . In reality, \mathcal{P} slowly changes in time, which leads to the separatrix deformation and saddle point displacement, a phenomenon closely related to the separatrix splitting under perturbations in dynamical systems. In simple terms it can be understood here by observing that if a particle is about to cross the separatrix almost exactly through the hyperbolic point, it can still make an extra cycle by an infinitesimal (e.g. numerical round-off errors) orbit perturbation. The extra cycle will then have a finite ($\sim v \ln v$) effect on the particle dynamics. The effect is pronounced, since the period diverges when the particle approaches the separatrix:

$$T = \frac{\partial I}{\partial p} \simeq \frac{2\sqrt{2}}{p_s^2} \ln \frac{1}{1 - p\mathcal{P}}. \quad (3.31)$$

Here $1 - p\mathcal{P} \ll 1$ can be expressed through the time t using eqs.(B.4) and (B.6). This phenomenon is predominantly responsible for the discrepancies between the analytic and numerical calculations shown in Fig.7. Further discussion can be found in Appendix B and in Sec.5.

4 Energy losses and other energetic constraints

Often, it is not the maximum energy of an accelerator which precludes the proton production with $E \gtrsim 10^{20}$ eV but the losses that either the accelerator cannot compensate for or exit

losses (i.e. caused by strong photon and/or magnetic fields, surrounding the acceleration zone) [14, 16, 42]. The DSA for example, is relatively slow because of the long idling time and, more importantly, it slows down with growing energy. Although the acceleration time may level off under certain circumstances, e.g. [43], it is unlikely to decrease with E and thus, the Synchrotron-Compton losses, for example, having the loss rate $\propto E$ (so that $\dot{E} \propto -E^2$) will ultimately prevail. Aside from that, the operation of powerful accelerators is usually accompanied by the production of other forms of energy, such as magnetic and photon fields, that boost the Synchrotron-Compton losses.

Fortunately, the present acceleration mechanism rapidly speeds up towards the maximum energy, $\dot{p} = vp^2$, eq.(3.29). The maximum energy is reached when a particle crosses the separatrix at $p_{\max} = p_s$. Although the energy grows also beyond this point, its growth is very slow as the particle recedes from the filament so that the separatrix crossing may be considered as an abrupt end of the acceleration. It is extremely beneficial for the UHECR production to terminate the acceleration process in such a way; the synchrotron losses also drop abruptly as the particle is released into a void, where only a weak magnetic field is present.

The Synchrotron-Compton losses of a proton with an energy E can be written as

$$\dot{E}_{\text{sc}} = -\frac{2}{3} \frac{e^4}{m_p^4 c^7} B^2 E^2$$

where e and m_p denote the proton charge and mass. Using dimensionless variables introduced in Sec.3, we can add this term to eq.(3.10) as follows

$$\dot{p} = \frac{vp\vartheta}{rp} - \eta p^2 B^2. \quad (4.1)$$

Here the dimensionless loss rate is

$$\eta = \frac{2}{3} \left(\frac{m_e}{m_p} \right)^4 \frac{r_e R_B^2}{r_{g\infty}^3} \approx 3 \cdot 10^{-12} \left(\frac{R_B}{10\text{Mpc}} \right)^2 \left(\frac{B_\infty}{\text{nG}} \right)^3,$$

with the classical electron radius $r_e = e^2/m_e c^2$, the Bondi radius R_B , eq.(A.16), and $r_{g\infty} = m_e c^2 / e B_\infty$. Naturally, the losses may become important towards the end of acceleration as both p and B grow. As we know the acceleration term is close to $\dot{p} = vp^2$ at this point, eq.(3.30), so that from eq.(4.1) we find that the acceleration will proceed up to the maximum momentum $p = p_s$ if

$$\frac{B^2(r_s)}{B_\infty^2} < \frac{v}{\eta} \simeq 5 \cdot 10^7 \sqrt{\frac{T}{10^4\text{K}}} \left(\frac{B_\infty}{\text{nG}} \right)^{-3} \left(\frac{R_B}{10\text{Mpc}} \right)^{-2} \quad (4.2)$$

Here we have evaluated the parameter v , eq.(3.5), by simply taking it at the sonic point (and using the approximation of the flow and field compression between $r = \infty$ and $r = R_B$, (eq.[A.15]) as $v \simeq 4C_\infty/c$. Moreover, if we use our earlier estimate of the IGM magnetic field $\sim \text{nG}$ compressed to $\sim \mu\text{G}$ level, for example, the l.h.s. of the last inequality is $\sim 10^6$ and even a strong inequality in eq.(4.2) can be satisfied. Of course, R_B can be estimated as $R_B \sim GM_f/C_s^2$ but it can too be inferred from the simulations and used then in eq.(4.2).

Turning to the photo-pion losses on the CMB we note that, in contrast to the Synchrotron-Compton losses, it is essentially a threshold process. Moreover, the photo-pion losses strongly dominate the pair production losses above a few 10^{19}eV , so we may ignore the latter in the

energy range of our interest. In what follows, we will extensively utilize the analyses of [14, 44, 45]. In particular, for energies $E < 3 \cdot 10^{20}$ eV the following simplified representation of the loss term can be used

$$-\frac{\dot{E}}{E} \approx \frac{c}{l_\pi} e^{-E_{\text{th}}/E} \quad (4.3)$$

with $E_{\text{th}} = m_p m_\pi c^4 (1 + m_\pi/m_p) / 2kT \approx 3 \cdot 10^{20}$ eV and $l_\pi \simeq 10$ Mpc. Here m_π is the pion's rest mass and T is the 2.7K CMB radiation temperature. For higher energies $E \gg E_{\text{th}}$ a slightly lower value of $c/l_\pi \approx 1.8 \cdot 10^{-8} \text{yr}^{-1}$ may be adopted but, this energy range can hardly be reached by this acceleration mechanism.

The dimensionless acceleration rate at the final stage of acceleration can be written as $p^{-1}\dot{p} \simeq vp$, eq.(3.30). Combining this with eq.(4.3) and using the dimensionless variables, we obtain

$$\frac{\dot{p}}{p} = vp - \frac{R_B}{l_\pi} e^{-p_{\text{th}}/p} \quad (4.4)$$

where p_{th} is the dimensionless photo-pion threshold momentum E_{th}/c . The right hand side of this equation may either have two roots or none. Recalling that the particle gyroradius is normalized to R_B , we may write the condition for the latter case ($\dot{p}/p > 0$ for all p) as follows

$$v \frac{r_g(p_{\text{th}}) l_\pi}{R_B^2} > e^{-1} \approx 0.37$$

where $r_g(p_{\text{th}})$ is the gyroradius of a proton with the momentum $p = p_{\text{th}}$ in the B_∞ magnetic field. Using our estimate $v \simeq 4C_\infty/c$ once again, the last condition rewrites

$$\frac{C_\infty}{c} > 3 \cdot 10^{-3} \left(\frac{R_B}{10 \text{Mpc}} \right)^2 \left(\frac{B_\infty}{\text{nG}} \right). \quad (4.5)$$

This requirement does not seem to be totally unrealistic particularly for flows with $T \sim 10^6 - 10^7 K$ heated by strong external shocks in the structure formation [25, 37]. Most likely it is marginally violated, so that the two roots of the expression on the r.h.s of eq.(4.4) do exist and significant photo-pion losses occur between these energies. It should also be recognized that higher maximum energy in eq.(3.28) makes the inequality in eq.(4.5) more difficult to satisfy in terms of parameters, such as C_∞ and B_∞ . The environments where the both requirements can be met should not be very common.

Overall, due to the fast energy gain in the betatron acceleration phase, the energy losses that are fatal for the DSA may be overcome. We therefore conclude that the maximum energy is likely to be determined by intrinsic limitations of the acceleration mechanism and not by the energy losses. The intrinsic acceleration limit is set by either the separatrix crossing or by reaching the flow deflection inside the filament, whichever occurs first.

Even though the calculation of the shape of the spectrum is beyond the scope of this paper, the key points of such calculation are worth mentioning here. First of all, the inverse-square relation between the initial and final particle momentum, eq.(3.25), suggests flipping the injected spectrum with respect to the fixed point of the map $p_0 \mapsto p_s$, given by (eq.[3.25]). Obviously, the fixed point of the map is $p = (0.25B_0)^{1/3}$. If the injection spectrum has the form $f_{\text{inj}} \propto p^{-q}$, for example, and it should be taken in the interval $0.5\sqrt{B_0}r_t^{1/4} < p <$

$(0.25B_0)^{1/3}$, then the accelerated particle spectrum will cover the interval $(0.25B_0)^{1/3} < p < r_t^{-1/2} = p_{\max}$, with an index $q' = q/2$. However, at least three obvious phenomena can steepen the spectrum substantially. First, as the particle momentum approaches p_{\max} , its orbit crosses and recrosses the circle of the radius r_t , and the odds for particle convection with the flow towards one of the nodes progressively increase. Second, the boundary between the radial and axial accretion at $r = r_t$ is not sharp. Therefore, one should not expect a sharp spectrum cut-off at p_{\max} but rather its decline starting at lower momenta. Finally, the photo pion losses that should be relatively strong for particles with momenta between the two roots of the r.h.s. of eq.(4.4) will modify the spectrum substantially. These phenomena may easily compensate for the spectrum hardening, produced by the inverse-square relation between initial and final momenta. Nevertheless, the kink at $p = (0.25B_0)^{1/3}$ may be pronounced. It should be noted here that energy-losses, such as the pair production losses and photo pion losses, have already been suggested to be responsible for such universal features in the UHECR energy spectrum as the dip and the bump [46].

A useful test of accelerator's potential is the energy dissipation rate by the emf (electromotive force) required for the acceleration of particles to the energy E_{\max} , subjected to the vacuum impedance $Z_0 \sim 10^2 \Omega$ [e.g., 13, 47]. Specifically, this power is $L_{\min} \sim \mathcal{E}^2/Z_0$, with the induction in the case of our interest $\mathcal{E} = 2\pi r E_\theta = 2\pi r u B/c = 2\pi v B_\infty R_B$. This quantity, in contrast to the most acceleration schemes, where $\mathcal{E} \sim E_{\max}/e$, is not related to E_{\max} because E_{\max} is independent of the accelerator power v , Sec.3.1. The reason for this is that in the betatron regime particles may pass through the accelerating field multiple times, and they will do it as many times as needed to reach the maximum energy. Indeed, according to eq.(3.11) we may write the dimensionless $p_{\max} \approx 2\pi n v$, where n is the number of rotations around the filament (orbit winding number), needed to reach p_{\max} . Therefore, returning to the dimensional units we can represent the induction also as $\mathcal{E} \sim E_{\max}/en$, and L_{\min} is thus reduced by n^2 , $L_{\min} \sim E_{\max}^2/e^2 n^2 Z_0$. On the other hand, the acceleration time does depend on the power v and a low-power source may fail to accelerate particles to the required energy for the energy loss reason.

5 Summary and Outlook

We have suggested a mechanism capable of proton re-acceleration to the maximum energy $\sim 10^{21}$ eV, provided that particles with energies $\gtrsim 10^{19}$ eV are seeded. These encouraging figures emerge for the plasma accretion on to a dark matter filament with the magnetic field compressed by a factor $\sim 10^3$, say from nG intergalactic field to μ G intracluster field. The required seed particles can arguably be pre-accelerated up to $\gtrsim 10^{19.5}$ eV by the standard diffusive shock acceleration (DSA) mechanism in the structure formation shocks [8, 14, 16] within the same accretion flow. Another important advantage of the suggested mechanism over, e.g., the DSA, is its very high rate during the end phase of acceleration, when particles usually suffer catastrophic losses.

The calculation of the spectrum of accelerated particles and acceleration efficiency is deferred to a future study. However, some of the ignored phenomena, such as magnetic field perturbations, merit a brief discussion. The magnetic field perturbations can scatter particles into the loss cones of the magnetic mirrors, presumably supported by the accreting nodes at the ends of the filament. However, since the final stage of acceleration (roughly the top decade in energy) is very short, relaxing our assumption $p_{\parallel} \ll p$ will not result in significant particle losses along the filament before they are expelled radially. More serious

are possible losses of seed particles during the slow drift phase between the node and filament radii, $R_f < r < R_n$, where $R_n \gtrsim R_f$ (Sec.2). While drifting towards the filament, the particles may diffuse to the nodes and disappear there without replenishment. The requirement on the radial flow velocity to avoid these losses is $u/c > R_n r_g / l^2$, where we have (somewhat arbitrarily) assumed the Bohm diffusion along the filament. Assuming also the gyroradius at the entrance $r_g \ll R_n \ll l$, the above condition does not seem to be unrealistic. Moreover, the loss of particles to the nodes may be compensated by the injection of high-energy particles accelerated in the nodes by, e.g., the DSA mechanism. Apart from the axial transport, the magnetic perturbations can result in the radial transport. The latter should also have a twofold impact on the acceleration. It can result in a premature expulsion of some particles from the accelerator but it can also prolongate the betatron phase of some other particles, thus increasing the maximum momentum.

One more factor which influences the duration of the betatron phase, is a sharply growing ($\propto r^{-\nu}$, with $\nu > 1$) magnetic field at small r . This is justified when a particle is expelled from the filament vicinity before reaching the filament axis where the magnetic field changes its r -dependence to remain finite at the origin. In terms of the dynamical system given by eqs.(3.15-3.17), the saddle point $r = r_s$ corresponds to an unstable periodic (circular) orbit of the full system of eqs(3.6-3.9) with $v = 0$. If the magnetic field decays slower than $1/r$ ($\nu < 1$) at the fixed point $r = r_s$, this circular orbit becomes stable. We have not considered particle acceleration in this regime for the reason that such particles are likely to be removed from the acceleration zone with the flow along the filament, that is by the process not studied in the paper. On the other hand, the change of stability of the fixed point should also retain orbits and enhance the energy.

Perhaps more important is the possible impact of perturbations on the motion near the separatrix, which is the most productive phase of this acceleration scheme. Recall that the particle orbit contracts to the filament axis during the betatron phase of acceleration. Clearly, this cannot continue infinitely so that upon approaching the separatrix, and the unstable hyperbolic point in particular, the particle slings out of the filament with all the energy gained during the orbit contraction. However, there is a phenomenon of stochastic layer formation in phase space near a separatrix. It results from perturbed particle dynamics closely related to the famous Poincaré's separatrix splitting, e.g., [48]. In general, the stochastic particle motion near the separatrix renders the particle exit moment, and thus the maximum energy, only statistically predictable, as opposed to our deterministic treatment in Sec.3 (see particularly the end of Sec.3.2 and Fig.7). Note that the magnetic field perturbations, that can easily randomize particle trajectory, do not have to be unstable or turbulent. The first azimuthal mode, that is carried over (even though suppressed) from an ambient magnetic field which is inclined with respect to the filament, but otherwise perfectly homogeneous, A.3, would suffice to create the stochastic layer.

We may conclude from the last remark that the mechanism requires a good magnetic field alignment with the filament direction. Despite the ubiquity of filaments in the large scale cosmic structure, only a small fraction of them may qualify for an efficient and visible accelerator. This needs to be taken into account when considering the observed correlation of the highest energy CRs with the distribution of the large-scale structure. In addition to the field alignment, the filament should be close to the plane of the sky, as the direction perpendicular to the filament is preferable for the acceleration. Unfortunately, for simple geometry reasons the filaments are more easily observed (as X-ray emitting gas) in the opposite case of the line-of-sight alignment, e.g. [40]. A more detailed phenomenology discussion

would be too speculative at this stage, but given the ongoing debates on the UHECR arrival anisotropy, e.g., [2, 49–54], the obvious angular characteristics of the suggested filament accelerator are worth mentioning. Evidently, a monoenergetic particle beam should fill a line of the angular length $\sim L/D$ in the filament direction, where $L \ll D$ is the length of the filament and D is the distance to the observer. In the perpendicular direction (orbit plane), the arrival direction should make an energy dependent angle α with respect to the line of sight to the filament, $\sin \alpha \simeq \alpha \simeq 2(R_B/r_g) \left[\sqrt{R_B/D} + D/4R_B \right]$, where the accretion radius is assumed to be much smaller than the particle gyroradius $R_B \ll r_g$. The above relation for α may be obtained from the conservation of particle canonical momentum $\mathcal{P} = \mathcal{P}_s$ after crossing the separatrix, Sec.3.

Overall, a particle acceleration by this mechanism to the up to date record energy of a few 10^{20} eV and its expulsion into the observer’s direction may be exceptional but possible. The above constraints, however, may be useful in explaining the Centaurus event excess under the absence of the Virgo events.

A Details of the flow and magnetic field structure

A.1 Dark matter gravitational potential

To describe the plasma accretion onto a filamentary structure outlined in Sec.2, we need to specify the gravitational potential of this structure. As we already mentioned, the DM particles interact collectively through the gravitational potential Φ that is governed by the Poisson equation

$$\Delta\Phi = 4\pi G\rho_{\text{DM}} \quad (\text{A.1})$$

where ρ_{DM} is the DM mass density. Furthermore, we assume that the system has already reached a “quasi-equilibrium” in terms of an appropriate coarsegraining [55–57] and this self-gravitating system may be described by a stationary Vlasov equation. The isotropic in velocity space solution amounts to a hydrostatic equilibrium

$$\nabla P_{\text{DM}} = -\rho_{\text{DM}}\nabla\Phi \quad (\text{A.2})$$

where P_{DM} is the DM pressure. Various approaches to the closure problem of the above equations have been suggested in the literature, including the recent unified DM model [e.g., 58]. For our purposes it is, perhaps, sufficient to assume a simple polytrope $P_{\text{DM}} = P_0(\rho_{\text{DM}}/\rho_0)^{\gamma_{\text{DM}}}$, where index 0 refers to the pressure and density values at the origin. Normalizing the spatial scale to

$$L = \frac{C_{\text{DM}}}{\sqrt{4\pi G(\gamma_{\text{DM}} - 1)\rho_0}}, \quad (\text{A.3})$$

where $C_{\text{DM}}^2 = \gamma_{\text{DM}}P_0/\rho_0$, and introducing $\theta^n = \rho_{\text{DM}}/\rho_0$ with $n = 1/(\gamma_{\text{DM}} - 1)$, we combine eqs.(A.1) and (A.2) into the following Emden-Fowler equation

$$\frac{1}{r^{d-1}} \frac{\partial}{\partial r} r^{d-1} \frac{\partial \theta}{\partial r} = -\theta^n \quad (\text{A.4})$$

where $d = 2, 3$ for cylindrically and spherically symmetric cases of our interest, both subjected to the boundary conditions $\theta(0) = 1, \theta'(0) = 0$. This equation was studied long time ago,

including the case of self-gravitating cylinder [59], where a series in power of r was obtained for an arbitrary n .

In choosing the suitable value for the index n , the superset Vlasov-Boltzmann equation for the DM distribution may be used

$$\frac{\partial f}{\partial t} + \mathbf{v} \cdot \nabla f - \nabla \Phi \cdot \frac{\partial f}{\partial \mathbf{v}} = 0 \quad (\text{A.5})$$

The ‘‘quasi-equilibrium’’ solution should depend on the energy integral $\epsilon = v^2/2 + \Phi$. Note that we assume the independence of the solution of the angular momentum (e.g., [60]). Assuming an equipartition in energy that runs from the bottom of the potential well $\epsilon_{min} = \min_r \Phi(r)$ to $\epsilon_{max} < 0$, it is straightforward to show that in the 3D case (gravitating node), the relation between the DM density and pressure is $P_{DM} \propto \rho_{DM}^{5/3}$, thus implying $\gamma_{DM} = 5/3$ and $n = 3/2$. In 2D (cylindrical symmetry) one obtains $\gamma_{DM} = 2$, $n = 1$. The latter case is particularly simple as the solution of eq.(A.4) is given by a Bessel function $J_0(r)$ for $r < j_{01} \simeq 2.4$, $J_0(j_{01}) = 0$.

However, as the nature of DM is unknown, we also apply for comparison the conventional $\gamma_{DM} = 5/3$ polytrope to the case of cylindrical symmetry. Note that a closed form solution of eq.(A.4) is not possible in the case $n = 3/2$, since the solution clearly has a movable pole of the form $\theta \propto 400(r - a)^{-4}$, where a is a constant. The pole and the zero of $\theta(r)$ at finite r (compact mass distribution), suggest the following Padé approximant (for the both symmetries)

$$\theta = \frac{1 - r^2/a_d^2}{1 + r^2/b_d^2} \quad (\text{A.6})$$

For $a_2 \approx 2.64$, $b_2 \approx 2.99$ (gravitating cylinder) and $a_3 \approx 3.6$, $b_3 \approx 3.2$ (gravitating sphere), the above approximation accurately reproduces the solution of eq.(A.4) for $n = 3/2$. It is shown in Fig.9 along with the numerical solution of eq.(A.4). We note that there is no significant difference between the $n = 3/2$ and $n = 1$ cases, where the latter may also be appropriate for the cylindrical symmetry.

Given the filament mass M_f , from eqs.(A.1,A.4) we obtain the following expression for C_{DM} in eq.(A.3):

$$C_{DM}^2 = (\gamma_{DM} - 1) \frac{GM_f}{\theta_* l}$$

where $\theta_* = -a_2 \theta'(a_2) \approx 1.12$, and $2l$ is the filament length.

It should be clear that the ‘dumbbell’ structure, shown in Fig.1, can be described by combining the spherical and cylindrical solutions, given by eq.(A.6), only approximately. Note that a_2 is identified with R_f - the filament radius and a_3 with the R_n - the node radius. At a minimum, a transition region between the two solutions should be addressed to match them. Even if the compound solution is constructed, the ‘dumbbell’ cannot be in exact equilibrium as an isolated self-gravitating structure. However, as a part of larger assembly of similar structures, the dumbbell may be considered to be stable.

With the above reservations in mind and, being interested primarily in the behavior of the gravitational potential in the middle part of the filament (i.e. not too close to the nodes, but with a reasonably accurate description of also the radially remote part of the solution, $r \gg l$), the gravitational potential of an isolated ‘dumbbell’ can be written down as follows

(we use the cylindrical coordinates with a z - axis along the filament, and with the node centers at $z = \pm l$, Fig.1):

$$\Phi(r, z) = \begin{cases} -\frac{GM_f}{\theta_* l} \theta(r) + \Phi_e(R_f, z), & r < R_f, |z| < l - R_n \\ \Phi_e(r, z), & r \geq R_f \end{cases} \quad (\text{A.7})$$

Here the function $\theta(r)$ and parameter θ_* may be chosen according to either $n = 3/2$ or $n = 1$ DM model, as discussed above. Quantitatively, the difference between them is not significant, so it is sufficient to adopt $n = 3/2$ value, for example. Furthermore, the function Φ_e (specified below) which represents the gravitational potential outside of the filament, i.e. in the region where significant part of particle energy is gained, does not depend on the exact distribution of the gravitational potential inside the filament. Since Φ_e represents the overall $\Phi(r, z)$ outside of the filament edge at $r = R_f$, and since $\theta(R_f) = 0$, the function Φ_e can be written down as follows

$$\Phi_e(r, z) = -\frac{GM_f}{2l} \sum_{\pm} \sinh^{-1} \left(\frac{l \pm z}{r} \right) - G \sum_{\pm} \frac{M_n}{\sqrt{r^2 + (z \pm l)^2}} \quad (\text{A.8})$$

Here the first term is the gravitational potential of the filament with the total mass M_f and length $2l$, while the second term represents the contribution of two nodes of equal masses M_n at the both ends of the filament. What is important for our present purposes, is the behavior of Φ near the mid-plane $z = 0$, inasmuch we will consider particle acceleration primarily in this area. So, in what follows we set $z = 0$ in the last equation, and neglect the gravitational pull from the both nodes, for simplicity.

A.2 Plasma flow towards filament

Having obtained the gravitational potential around a 'dumbbell' structure, we now concern with the plasma accretion onto it. The Bernoulli integral for the flow reads

$$\frac{u^2}{2} + \frac{C_\infty^2}{\gamma - 1} \left[\left(\frac{\rho}{\rho_\infty} \right)^{\gamma - 1} - 1 \right] + \Phi = 0 \quad (\text{A.9})$$

Using the cylindrical coordinates, $u = \sqrt{u_r^2 + u_z^2} \simeq u_r$ is the gas flow speed, ρ is its density with $\rho = \rho_\infty$ at $r = \infty$, γ is the gas adiabatic index, and $C_\infty = \sqrt{\gamma P_\infty / \rho_\infty}$ is the sound velocity at infinity. A brief comment about the overall geometry of the flow is in order here. If we consider the dumbbell as an isolated structure, then the flow speed at infinity $u \propto 1/r^2$. If, on the other hand, the dumbbell is part of an extended elongated structure, or if the sonic point (Bondi radius) at $r = R_B$ is located not far away from the filament, $R_B \sim l$, then the relation $u \propto 1/r$ better represents the flow at large distances. To encompass the both options we set the accretion flux

$$\rho u_r r^{d-1} = J = \dot{M} / 2 (d - 1) \pi \quad (\text{A.10})$$

where \dot{M} is the spherical accretion rate ($d = 3$) or the accretion rate per unit length of the filament ($d = 2$). Using the results of the preceding subsection, the Bernoulli integral given by eq.(A.9) can be re-written as follows

$$\frac{1}{2} \mathcal{M}^{4/(\gamma+1)} + \frac{1}{\gamma - 1} \mathcal{M}^{-2(\gamma-1)/(\gamma+1)} = \lambda \left(\frac{r}{l} \right)^\mu \left(1 + \zeta \sinh^{-1} \frac{l}{r} \right) \quad (\text{A.11})$$

where we have used the following notations: $\mathcal{M} = (u_r/C_\infty) (\rho_\infty/\rho)^{(\gamma-1)/2}$ is the local Mach number,

$$\lambda = \frac{1}{\gamma-1} \left[\frac{C_\infty \rho_\infty}{u_B \rho_B} \left(\frac{l}{R_B} \right)^{d-1} \right]^{2(\gamma-1)/(\gamma+1)}, \quad (\text{A.12})$$

$$\mu = 2(d-1) \frac{\gamma-1}{\gamma+1}, \quad \zeta = (\gamma-1) \frac{GM_f}{lC_\infty^2} = \theta_* \frac{\gamma-1}{\gamma_{\text{DM}}-1} \frac{C_{\text{DM}}^2}{C_\infty^2}. \quad (\text{A.13})$$

and where $u_B = u(R_B)$, $\rho_B = \rho(R_B)$. The contour plot of eq.(A.11) is shown in Fig.10. As usual for the Bondi accretion, the flow passes through the sonic point R_B after which a shock may form. Evidently, our simplified model does not allow us to find the shock position accurately. Appealing to the Λ CDM simulations [18, 24, 61, 62] we may expect that the most probable shock strength in terms of its upstream Mach number is $\mathcal{M}_1 \sim 2-3$, as the strong shocks are located well outside of the region of our interest. The flow Mach number behind the shock can be determined using the standard formula

$$\mathcal{M}_2^2 = \frac{\gamma-1 + 2/\mathcal{M}_1^2}{2\gamma - (\gamma-1)/\mathcal{M}_1^2}$$

which allows us to determine the flow density and speed also for $r < R_B$ using the Bernoulli equation (A.11). In particular, for sufficiently small r , where $\mathcal{M} \ll 1$, the following simple expression for the plasma density may be used (see eq.[A.9])

$$\frac{\rho}{\rho_\infty} \simeq \left[1 + \zeta \sinh^{-1} \frac{l}{r} \right]^{1/(\gamma-1)} \quad (\text{A.14})$$

This representation of ρ can be used outside of the filament, $r > R_f$ while within the DM filament the situation is somewhat more complicated. Of course, the 'vacuum' gravitational potential $\Phi \propto \sinh^{-1}(l/r)$ should be replaced by $\Phi \propto \theta(r)$, according to eq.(A.7). At the same time, when the flow approaches the filament axis, it also turns into z -direction so that u_z component cannot be neglected compared to u_r in eq.(A.9). Clearly, our simplified treatment needs to be modified by addressing the flow in r and z variables in this case. However, we limit our consideration to the case when the particle gyroradius $r_g > R_t$, where R_t is the radius where $u_z \sim u_r$. Aiming at our treatment of the acceleration mechanism in Sec.3, we may expand the density profile in eq.(A.14) as

$$\rho/\rho_\infty \simeq (1 + R_B/r)^{1/(\gamma-1)}, \quad (\text{A.15})$$

which is valid for not too small $r \gtrsim l$, and where R_B is specified as follows

$$R_B = (\gamma-1) GM_f/C_\infty^2 \gg R_f > R_t. \quad (\text{A.16})$$

The simplification of the density profile using eq.(A.15) is roughly in agreement with eq.(A.14) even for small $r \ll l$, in the case of a softer but not unreasonable equation of state, $\gamma = 7/5$. For example, if r/l varies between 4 and 0.04, ρ/ρ_∞ grows from ~ 10 to 10^4 for $\zeta = 10$. Since the magnetic field component that is parallel to the filament is compressed as the density, the above three order of magnitude density compression over the two order of magnitude distance variation is consistent with the field compression between the nano-gauss intergalactic and micro-gauss intracluster field.

The parameter ζ in eq.(A.13), which can also be represented as $\zeta = R_B/l$, regulates the total density/magnetic field compression between the IGM and the acceleration termination zone at $r \sim R_t$. There are some observational constraints on C_{DM} in eq.(A.13) being $C_{DM} \lesssim C_{IC}$ [63], where C_{IC} is the intracluster gas thermal velocity. Thus, the value of ζ may depend on how cool the IGM gas is compared to the IC gas. This, in turn, would depend on whether strong external [24, 37] accretion shocks are present outside of R_B and heat the gas and it might be that, at least in some cases, $\zeta \sim 1$ or even smaller if cooling occurs in the shocked flow [41]. On the other hand, the expression for R_B , if the accretion flow originates at a distance $\gtrsim l$, should be modified by replacing M_f in eq.(A.16) by the total mass of the 'dumbbell' as an accreting entity. This can considerably increase R_B and ζ . Equally important may be strong modification of the external shocks by accelerated CRs, e.g., [64], so that the 'subshock' Mach number would decrease substantially and so the shock heating rate would drop as well, e.g. [65, 66].

A.3 Magnetic field around filaments and nodes

We assume that the magnetic field is passively transported from the filament surroundings with the accretion flow. For simplicity, we consider the field profile created by this process around each of the two nodes and around the filament separately. This will provide some insight into how the field around the dumbbell structure may be organized. Given the initial field distribution $\mathbf{B}(\mathbf{r}, 0)$ and the velocity field $\mathbf{u}(\mathbf{r}, t)$, the magnetic field $\mathbf{B}(\mathbf{r}, t)$ can be obtained in terms of Lagrangian variables [67].

A.3.1 Magnetic Field around Nodes

Starting with the node accretion and using the spherical coordinates r, ϑ, ϕ centered in one of the nodes, we assume that the magnetic field and the flow velocity can be represented as $\mathbf{B}(r) = (B_r, B_\vartheta, 0)$ and $\mathbf{u}(r) = (u_r, 0, 0)$, respectively. Note that the polar axis here may or may not coincide with the direction of the filament. Using the field induction equation $\mathbf{B}_t = \nabla \times \mathbf{u} \times \mathbf{B}$, we obtain the following two equations for B_r and B_ϑ components

$$\frac{d}{dt} r^2 B_r = 0; \quad \frac{d}{dt} r u_r B_\vartheta = 0$$

with

$$\frac{d}{dt} \equiv \frac{\partial}{\partial t} + u_r \frac{\partial}{\partial r}. \quad (\text{A.17})$$

We assume the magnetic field being initially constant everywhere and directed along the polar axis. Therefore, at $t = 0$ we have $B_r(0) = B_0 \cos \vartheta$ and $B_\vartheta(0) = -B_0 \sin \vartheta$. Introducing a new variable

$$\tau = - \int_0^r \frac{dr}{u_r(r)}, \quad (\text{A.18})$$

we can write the solution for \mathbf{B} as follows

$$B_\vartheta(t, r, \vartheta) = -B_0 \frac{\mathcal{F}[\tau(r) + t]}{r u_r(r)} \sin \vartheta \quad (\text{A.19})$$

$$B_r(r, t, \vartheta) = B_0 \frac{\mathcal{G}[\tau(r) + t]}{r^2} \cos \vartheta \quad (\text{A.20})$$

where \mathcal{F} and \mathcal{G} are defined by the following relations: $\mathcal{F}[\tau(r)] = ru_r(r)$, $\mathcal{G}[\tau(r)] = r^2$. Time asymptotically ($t \rightarrow \infty$, $r < \infty$) the field becomes purely radial almost everywhere (except for the equatorial plane $\vartheta = \pi/2$). The reason for such behavior is that $\mathcal{F}(\tau)$ reaches its maximum at $\tau \sim \tau_B \equiv \tau(R_B)$ and then decays, since $u_r \sim 1/r^2$ as $r \rightarrow \infty$, whereas $\mathcal{G}(\tau)$ is unbounded. From the physical point of view, the effective radius from which the material is accreted should be limited by $r \lesssim R_B$ or, equivalently, the argument in expressions given by eqs.(A.19-A.20) should be limited by $\tau(r) + t \lesssim \tau_B$. In addition, the magnetic field compression outside of the sonic radius $r = R_B$ is not significant. Further details about the magnetic field geometry depend on whether or not shocks are formed in the flow. It should be noted that spherically accreting monoatomic gas cannot become supersonic since the sonic point $R_B \rightarrow 0$ for $\gamma = 5/3$ [68, 69] (this may be seen from the Bernoulli equation). However, there are possibilities for the gas to be shocked. First, a diatomic index $\gamma = 7/5$ may be a better choice than the $\gamma = 5/3$ index. Second, there may be a softer equation of state, $\gamma < 5/3$, if there is a significant component of accelerated cosmic rays [20, 70] so that the relativistic gas index $\gamma = 4/3$ may be a better approximation. If the flow does become supersonic, we can estimate from eq.(A.9) $u_r \propto \Phi^{1/2} \sim r^{-1/2}$ (free fall accretion regime). If, on the other hand, the flow remains ($\gamma = 5/3$) or becomes ($\gamma < 5/3$) subsonic after being shocked, we can write $u_r \propto r^{(3-2\gamma)/(\gamma-1)}$ and $B_\vartheta(r, \vartheta) = B_\vartheta(r_{\text{sh}}, \vartheta) (r_{\text{sh}}/r)^{(2-\gamma)/(\gamma-1)}$, where r_{sh} is the shock stand-off radius and $B_\vartheta(r_{\text{sh}}, \vartheta)$ is the magnetic field behind the shock. The latter can be obtained using the standard shock formulae, given the field ahead of the shock. The radial component of the magnetic field is simply $B_r(r, \vartheta) = B_r(r_{\text{sh}}, \vartheta) (r_{\text{sh}}/r)^2$. We may see that in the both cases the magnetic field becomes essentially radial due to the conservation of the flux $r^2 B_r$ in converging flow.

A.3.2 Magnetic field around filament

Turning to the filament part of the flow, we use the cylindrical coordinate with an axis z along the filament and assume that the initial magnetic field has all three components $\mathbf{B} = (B_r, B_\vartheta, B_z)$. From the induction equation with a cylindrical flow in radial direction, $\mathbf{u} = (u_r, 0, 0)$ we obtain

$$\frac{d}{dt} r B_r = 0; \quad \frac{d}{dt} u_r B_\vartheta = 0; \quad \frac{d}{dt} r u_r B_z = 0$$

where, again, $d/dt = \partial/\partial t + u_r \partial/\partial r$. As in the spherical case, the solutions of these equations can be written down in terms of the characteristics given by equations formally identical to eqs.(A.17-A.18). For our purposes, it is sufficient to realize that $B_\vartheta/B_z \propto r$ and $B_r/B_z \propto u_r$. As far as the B_ϑ component is concerned, the alignment between the magnetic field and the filament clearly improves towards the axis. Turning to B_r/B_z ratio we note, that it grows as the flow approaches the filament upstream of a shock, should the latter occur in the flow. At the same time, this quantity should decay in the shocked flow, if the density (and thus the B_z component) grows fast enough with decreasing r . As we have argued in the preceding subsection, an $\propto r^{-3/2}$ scaling of the density is a reasonable approximation. Therefore, we deduce that $B_r/B_z \propto r^{1/2}$, which is a substantial reorientation of the ambient magnetic field in the filament direction during its convection into the filament.

We thus conclude this section with i.) magnetic field is compressed near the nodes stronger than near the filament, thus creating magnetic mirrors for particles accelerated around the filament, and ii.) the field is well aligned along the filament, if it is reasonably

aligned with it outside of the accretion region. These results are essential for the particle acceleration mechanism which we describe in Sec.3.

B Adiabatic invariant near separatrix

In order to calculate the time dependence of particle momentum at the final stage of acceleration, we transform the expression for the adiabatic invariant, given by eq.(3.19), to the following form

$$I = 2\mathcal{P} \oint \sqrt{\lambda^2 - (x-1)^2/x^4} dx. \quad (\text{B.1})$$

Here we have used the magnetic field from eq.(3.20) (with $\nu = 3/2$) along with the variable $x = 2\sqrt{r}/\mathcal{P}$. We also have introduced a new variable $\lambda = p\mathcal{P}/4$ that takes $\lambda = 1/4$ value at the separatrix. The last integral may be done in terms of elliptic integrals but, as this expression involves the elliptic integral of the third kind, it is not practical to do so. Since we are primarily interested in the particle motion near the separatrix, it is easier to describe this motion using eq.(B.1) directly. Noting that $I(\lambda)$ has a singular contribution from its upper limit (separatrix) $x \rightarrow 2$ as $\lambda \rightarrow 1/4$, we calculate $\partial I/\partial\lambda^2$ instead of I , to make the contribution from this point well expressed. The integral $I(\lambda)$ will be then easily restored, as we know its value at $\lambda = 1/4$, eq.(3.23). Keeping $\mathcal{P} = \text{const}$, eq.(B.1) may be manipulated into

$$\frac{\partial I}{\partial\lambda^2} = 2\frac{\mathcal{P}}{\lambda^3} \int_a^{1-\sqrt{1/2-a^2}} \frac{(1/2-z)^3}{\sqrt{z^2-a^2}\sqrt{z^2-2z+a^2+1/2}} dz, \quad (\text{B.2})$$

where we have introduced another variable

$$a^2 = \frac{1}{4} - \lambda = \frac{1-p\mathcal{P}}{4},$$

so that the singular turning point now appears at the lower limit of the integral as $a \rightarrow 0$. Near the separatrix, i.e. for $a \ll 1$, the main contribution to the last integral can be evaluated as follows

$$\frac{\partial I}{\partial\lambda^2} = \frac{\sqrt{2}}{4} \frac{\mathcal{P}}{\lambda^3} \cosh^{-1} \frac{1}{a} + \mathcal{O}(1)$$

Taking eq.(3.23) into account, we obtain the following expression for the adiabatic invariant which is strictly valid for the motion near the separatrix

$$I(p, \mathcal{P}) = \mathcal{P} \left[2 \left(4 \ln \frac{1}{\sqrt{2}-1} - \pi \right) + \sqrt{2} (1-p\mathcal{P}) \ln (1-p\mathcal{P}) + \mathcal{O}(1-p\mathcal{P}) \right] \quad (\text{B.3})$$

To explicitly find the time dependence of the particle momentum from this expression, we write

$$I(p, \mathcal{P}(t)) \approx I_s = \text{const}$$

and introduce the following variable ε , which characterizes the orbit proximity to the separatrix

$$\varepsilon(t) = \frac{I_s}{\sqrt{2}} \left(p_s - \frac{1}{\mathcal{P}} \right) \ll 1. \quad (\text{B.4})$$

Now eq.(B.3) takes the following compact form

$$(1 - p\mathcal{P}) \ln(1 - p\mathcal{P}) + \varepsilon = 0. \quad (\text{B.5})$$

Recall that \mathcal{P} is a known function of time: $\mathcal{P}(t) = \mathcal{P}_0 - vt$. Eq.(B.5) can be explicitly solved for $p(t)$ using the following recursive expression

$$p(\mathcal{P}) = \frac{1}{\mathcal{P}} \left[1 - \frac{\varepsilon}{\ln\left(\frac{1}{\varepsilon} \left(\ln\frac{1}{\varepsilon} \dots\right)\right)} \right] \quad (\text{B.6})$$

Note that this solution is valid for $1 - p\mathcal{P} \leq 1/e$, which is certainly fulfilled in the case of our interest. The logarithm recursive expression converges to the solution of eq.(B.5) in this case, and it is sufficient to truncate it after 3-4 iterations. Fig.6 shows the final stage of acceleration, obtained by direct numerical integration. For comparison, $p(t)$ from eq.(B.6), truncated after four iterations, is also shown.

As we mentioned earlier, the growth of the particle momentum with time is explosive near the separatrix. Indeed, from the last equation with $\varepsilon \ll 1$, we obtain eq.(3.29). We also note here, that in calculating the acceleration time in eq.(3.30), we neglected terms $\sim 1/\ln(1/\varepsilon)$ compared to unity which is consistent with the accuracy of the above calculations.

References

- [1] G. Sigl, F. Miniati, and T. A. Ensslin, *Ultrahigh energy cosmic rays in a structured and magnetized universe*, *Phys. Rev. D* **68** (Aug, 2003) 043002.
- [2] E. Waxman and A. Loeb, *Constraints on the local sources of ultra high-energy cosmic rays*, *J. Cosmol. Astropart. Phys.* **8** (Aug., 2009) 26+, [[arXiv:0809.3788](#)].
- [3] The Pierre Auger Collaboration, J. Abraham, P. Abreu, M. Aglietta, C. Aguirre, D. Allard, I. Allekotte, J. Allen, P. Allison, C. Alvarez, and et al., *Correlation of the Highest-Energy Cosmic Rays with Nearby Extragalactic Objects*, *Science* **318** (Nov., 2007) 938–, [[arXiv:0711.2256](#)].
- [4] M. Takeda, N. Hayashida, K. Honda, N. Inoue, K. Kadota, F. Kakimoto, K. Kamata, S. Kawaguchi, Y. Kawasaki, N. Kawasumi, E. Kusano, Y. Matsubara, K. Murakami, M. Nagano, D. Nishikawa, H. Ohoka, S. Ozone, N. Sakaki, M. Sasaki, K. Shinozaki, N. Souma, M. Teshima, R. Torii, I. Tsushima, Y. Uchihori, T. Yamamoto, S. Yoshida, and H. Yoshii, *Small-Scale Anisotropy of Cosmic Rays above 10^{19} eV Observed with the Akeno Giant Air Shower Array*, *Astrophys. J.* **522** (Sept., 1999) 225–237, [[astro-ph/](#)].
- [5] Gopal-Krishna, P. L. Biermann, V. de Souza, and P. J. Wiita, *Ultra-high-energy Cosmic Rays from Centaurus A: Jet Interaction with Gaseous Shells*, *Astrophys. J. Lett.* **720** (Sept., 2010) L155–L158, [[arXiv:1006.5022](#)].
- [6] K. Kotera and A. V. Olinto, *The Astrophysics of Ultrahigh Energy Cosmic Rays*, *ArXiv e-prints* (Jan., 2011) [[arXiv:1101.4256](#)].
- [7] The Pierre Auger Collaboration, P. Abreu, M. Aglietta, E. J. Ahn, D. Allard, I. Allekotte, J. Allen, J. Alvarez Castillo, J. Alvarez-Muñiz, M. Ambrosio, and et al., *Update on the correlation of the highest energy cosmic rays with nearby extragalactic matter*, *ArXiv e-prints* (Sept., 2010) [[arXiv:1009.1855](#)].

- [8] H. Kang, D. Ryu, and T. W. Jones, *Cluster Accretion Shocks as Possible Acceleration Sites for Ultra-High-Energy Protons below the Greisen Cutoff*, *Astrophys. J.* **456** (Jan., 1996) 422–+, [[astro-ph/](#)].
- [9] M. Milgrom and V. Usov, *Possible Association of Ultra-High-Energy Cosmic-Ray Events with Strong Gamma-Ray Bursts*, *Astrophys. J. Lett.* **449** (Aug., 1995) L37+, [[astro-ph/](#)].
- [10] M. Vietri, *The Acceleration of Ultra-High-Energy Cosmic Rays in Gamma-Ray Bursts*, *Astrophys. J.* **453** (Nov., 1995) 883–+, [[astro-ph/](#)].
- [11] E. Waxman, *Cosmological Gamma-Ray Bursts and the Highest Energy Cosmic Rays*, *Physical Review Letters* **75** (July, 1995) 386–389.
- [12] G. R. Farrar and P. L. Biermann, *Correlation between Compact Radio Quasars and Ultrahigh Energy Cosmic Rays*, *Physical Review Letters* **81** (Oct., 1998) 3579–3582.
- [13] R. D. Blandford, *Acceleration of Ultra High Energy Cosmic Rays*, *Phys.Scripta* **T85** (2000) 191–194.
- [14] C. A. Norman, D. B. Melrose, and A. Achterberg, *The Origin of Cosmic Rays above 10^{18.5} eV*, *Astrophys. J.* **454** (Nov., 1995) 60–+.
- [15] F. A. Aharonian, A. A. Belyanin, E. V. Derishev, V. V. Kocharovskiy, and V. V. Kocharovskiy, *Constraints on the extremely high-energy cosmic ray accelerators from classical electrodynamics*, *Phys. Rev. D* **66** (July, 2002) 023005–+.
- [16] T. W. Jones, *Ultra High Energy Cosmic Rays and Clusters*, *Journal of Korean Astronomical Society* **37** (Dec., 2004) 421–426.
- [17] D. F. Torres and L. A. Anchordoqui, *Astrophysical origins of ultrahigh energy cosmic rays.*, *Reports on Progress in Physics* **67** (2004) 1663–1730.
- [18] F. Miniati, D. Ryu, H. Kang, and T. W. Jones, *Cosmic-Ray Protons Accelerated at Cosmological Shocks and Their Impact on Groups and Clusters of Galaxies*, *Astrophys. J.* **559** (Sept., 2001) 59–69.
- [19] H. Kang and T. W. Jones, *Cosmic Ray Acceleration at Cosmological Shocks*, *Journal of Korean Astronomical Society* **37** (Dec., 2004) 405–412.
- [20] H. Kang and T. W. Jones, *Efficiency of Nonlinear Particle Acceleration at Cosmic Structure Shocks*, *Astrophys. J.* **620** (Feb., 2005) 44–58.
- [21] T. A. Enßlin, C. Pfrommer, V. Springel, and M. Jubelgas, *Cosmic ray physics in calculations of cosmological structure formation*, *Astronomy and Astrophysics.* **473** (Oct., 2007) 41–57, [[astro-ph/](#)].
- [22] C. Pfrommer, V. Springel, M. Jubelgas, and T. A. Ensslin, *Cosmic Ray Feedback in Hydrodynamical Simulations of Galaxy and Galaxy Cluster Formation*, [astro-ph/](#).
- [23] B. S. Sathyaprakash, V. Sahni, and S. F. Shandarin, *Emergence of Filamentary Structure in Cosmological Gravitational Clustering*, *Astrophys. J. Lett.* **462** (May, 1996) L5+, [[astro-ph/](#)].
- [24] D. Ryu, H. Kang, E. Hallman, and T. W. Jones, *Cosmological Shock Waves and Their Role in the Large-Scale Structure of the Universe*, *Astrophys. J.* **593** (Aug., 2003) 599–610.
- [25] R. Cen and J. P. Ostriker, *Where Are the Baryons? II. Feedback Effects*, *Astrophys. J.* **650** (Oct., 2006) 560–572, [[astro-ph/](#)].
- [26] F. Vazza, G. Brunetti, C. Gheller, and R. Brunino, *Massive and refined: A sample of large galaxy clusters simulated at high resolution. I: Thermal gas and properties of shock waves*, *New Astronomy* **15** (Nov., 2010) 695–711, [[arXiv:1003.5658](#)].
- [27] B. Aracil, T. M. Tripp, D. V. Bowen, J. X. Prochaska, H. Chen, and B. L. Frye, *High-metallicity, photoionized gas in intergalactic large-scale filaments*, *Mon. Not. R. Astron.*

- Soc.* **367** (Mar., 2006) 139–155, [[astro-ph/](#)].
- [28] A. Zitrin and N. Brosch, *The NGC 672 and 784 galaxy groups: evidence for galaxy formation and growth along a nearby dark matter filament*, *Mon. Not. R. Astron. Soc.* **390** (Oct., 2008) 408–420, [[arXiv:0808.1789](#)].
- [29] R. Z. Sagdeev, “Shock” waves in rarefied plasma, in *Ionization Phenomena in Gases, Volume II* (N. R. Nilsson, ed.), pp. 1081–+, 1960.
- [30] E. Schatzman, *On the acceleration of particles in shock fronts*, *Annales d’Astrophysique* **26** (Feb., 1963) 234–+.
- [31] M. A. Lee, V. D. Shapiro, and R. Z. Sagdeev, *Pickup ion energization by shock surfing*, *J. Geophys. Res.* **101** (Mar., 1996) 4777–4790.
- [32] G. P. Zank, H. L. Pauls, I. H. Cairns, and G. M. Webb, *Interstellar pickup ions and quasi-perpendicular shocks: Implications for the termination shock and interplanetary shocks*, *J. Geophys. Res.* **101** (Jan., 1996) 457–478.
- [33] I. N. Toptygin, *Acceleration of particles by shocks in a cosmic plasma*, *Space Science Reviews* **26** (June, 1980) 157–213.
- [34] L. O. Drury, *An introduction to the theory of diffusive shock acceleration of energetic particles in tenuous plasmas*, *Reports on Progress in Physics* **46** (Aug., 1983) 973–1027.
- [35] K. Dolag, D. Grasso, V. Springel, and I. Tkachev, *Constrained simulations of the magnetic field in the local Universe and the propagation of ultrahigh energy cosmic rays*, *J. Cosmol. Astropart. Phys.* **1** (Jan., 2005) 9–+, [[astro-ph/](#)].
- [36] M. Boylan-Kolchin, V. Springel, S. D. M. White, A. Jenkins, and G. Lemson, *Resolving cosmic structure formation with the Millennium-II Simulation*, *Mon. Not. R. Astron. Soc.* **398** (Sept., 2009) 1150–1164, [[arXiv:0903.3041](#)].
- [37] F. Miniati, D. Ryu, H. Kang, T. W. Jones, R. Cen, and J. P. Ostriker, *Properties of Cosmic Shock Waves in Large-Scale Structure Formation*, *Astrophys. J.* **542** (Oct., 2000) 608–621, [[astro-ph/](#)].
- [38] P. Blasi, *Cosmic Ray Acceleration During Large Scale Structure Formation*, *Journal of Korean Astronomical Society* **37** (Dec., 2004) 483–491.
- [39] K. Dolag, M. Meneghetti, L. Moscardini, E. Rasia, and A. Bonaldi, *Simulating the physical properties of dark matter and gas inside the cosmic web*, *Mon. Not. R. Astron. Soc.* **370** (Aug., 2006) 656–672, [[astro-ph/](#)].
- [40] N. Werner, A. Finoguenov, J. S. Kaastra, A. Simionescu, J. P. Dietrich, J. Vink, and H. Böhringer, *Detection of hot gas in the filament connecting the clusters of galaxies Abell 222 and Abell 223*, *Astronomy and Astrophys.* **482** (May, 2008) L29–L33, [[arXiv:0803.2525](#)].
- [41] A. C. Fabian, *Cooling Flows in Clusters of Galaxies*, *ARA&A* **32** (1994) 277–318.
- [42] A. Levinson, *Particle Acceleration and Curvature TeV Emission by Rotating, Supermassive Black Holes*, *Physical Review Letters* **85** (July, 2000) 912–915.
- [43] M. A. Malkov and P. H. Diamond, *Nonlinear Shock Acceleration Beyond the Bohm Limit*, *Astrophys. J.* **642** (2006) 244–259.
- [44] V. S. Berezhinskii, S. V. Bulanov, V. A. Dogiel, and V. S. Ptuskin, *Astrophysics of cosmic rays*. Amsterdam: North-Holland, 1990.
- [45] V. S. Berezhinskii and S. I. Grigor’eva, *A bump in the ultra-high energy cosmic ray spectrum*, *Astronomy and Astrophys.* **199** (June, 1988) 1–12.
- [46] V. Berezhinsky, A. Gazizov, and S. Grigorieva, *On astrophysical solution to ultrahigh energy cosmic rays*, *Phys. Rev. D* **74** (Aug., 2006) 043005–+, [[hep-ph/02](#)].

- [47] G. Sigl, *Time structure and multi-messenger signatures of ultra-high energy cosmic ray sources*, *New Journal of Physics* **11** (June, 2009) 065014–+.
- [48] G. M. Zaslavsky, R. Z. Sagdeev, D. A. Usikov, and A. A. Chernikov, *Weak Chaos and Quasi-Regular Patterns*. Cambridge University Press, 1991.
- [49] M. R. George, A. C. Fabian, W. H. Baumgartner, R. F. Mushotzky, and J. Tueller, *On active galactic nuclei as sources of ultra-high energy cosmic rays*, *Mon. Not. R. Astron. Soc.* **388** (July, 2008) L59–L63, [[arXiv:0805.2053](#)].
- [50] G. Ghisellini, G. Ghirlanda, F. Tavecchio, F. Fraternali, and G. Pareschi, *Ultra-high energy cosmic rays, spiral galaxies and magnetars*, *Mon. Not. R. Astron. Soc.* **390** (Oct., 2008) L88–L92, [[arXiv:0806.2393](#)].
- [51] D. Gorbunov, P. Tinyakov, I. Tkachev, and S. Troitsky, *On the correlation of the highest-energy cosmic rays with nearby extragalactic objects reported by the Pierre Auger Collaboration*, *Soviet Journal of Experimental and Theoretical Physics Letters* **87** (July, 2008) 461–463, [[arXiv:0711.4060](#)].
- [52] D. Fargion, *UHECR besides Cen A : Hints of galactic sources*, *Progress in Particle and Nuclear Physics* **64** (Apr., 2010) 363–365, [[arXiv:0911.4176](#)].
- [53] S. Gureev and S. Troitsky, *Physical Conditions in Nearby Active Galaxies Correlated with Ultra-High Cosmic Rays Detected by the Pierre Auger Observatory*, *International Journal of Modern Physics A* **25** (2010) 2917–2932.
- [54] D. V. Semikoz, *Ultra-high energy nuclei source in the direction to Virgo cluster*, *ArXiv e-prints* (Sept., 2010) [[arXiv:1009.3879](#)].
- [55] D. Lynden-Bell, *Statistical mechanics of violent relaxation in stellar systems*, *Mon. Not. R. Astron. Soc.* **136** (1967) 101–+.
- [56] S. D. M. White and M. J. Rees, *Core condensation in heavy halos - A two-stage theory for galaxy formation and clustering*, *Mon. Not. R. Astron. Soc.* **183** (May, 1978) 341–358.
- [57] J. F. Navarro, C. S. Frenk, and S. D. M. White, *A Universal Density Profile from Hierarchical Clustering*, *Astrophys. J.* **490** (Dec., 1997) 493–+, [[astro-ph/](#)].
- [58] R. J. Scherrer, *Purely kinetic k essence as unified dark matter*, *Phys. Rev. Lett.* **93** (Jun, 2004) 011301.
- [59] J. Ostriker, *The Equilibrium of Polytropic and Isothermal Cylinders.*, *Astrophys. J.* **140** (Oct., 1964) 1056–+.
- [60] J. Calvo, E. Florido, O. Sánchez, E. Battaner, J. Soler, and B. Ruiz-Granados, *On a unified theory of cold dark matter halos based on collisionless Boltzmann-Poisson polytropes*, *Physica A Statistical Mechanics and its Applications* **388** (June, 2009) 2321–2330.
- [61] C. Pfrommer, V. Springel, T. A. Enßlin, and M. Jubelgas, *Detecting shock waves in cosmological smoothed particle hydrodynamics simulations*, *Mon. Not. R. Astron. Soc.* **367** (Mar., 2006) 113–131, [[astro-ph/](#)].
- [62] F. Vazza, G. Brunetti, and C. Gheller, *Shock waves in Eulerian cosmological simulations: main properties and acceleration of cosmic rays*, *Mon. Not. R. Astron. Soc.* **395** (May, 2009) 1333–1354, [[arXiv:0808.0609](#)].
- [63] Y. Ikebe, H. Böhringer, and T. Kitayama, *X-Ray Measurement of Dark Matter “Temperature” in A1795*, *Astrophys. J.* **611** (Aug., 2004) 175–185, [[astro-ph/](#)].
- [64] M. A. Malkov, P. H. Diamond, and H. J. Völk, *Critical Self-Organization of Astrophysical Shocks*, *Astrophys. J. Lett.* **533** (Apr., 2000) L171–L174.
- [65] M. A. Malkov, *Analytic Solution for Nonlinear Shock Acceleration in the Bohm Limit*, *Astrophys. J.* **485** (Aug., 1997) 638–654.

- [66] L. Drury, F. A. Aharonian, D. Malyshev, and S. Gabici, *On the plasma temperature in supernova remnants with cosmic-ray modified shocks*, *Astronomy and Astrophys.* **496** (Mar., 2009) 1–6, [[arXiv:0811.3566](#)].
- [67] H. K. Moffatt, *Magnetic field generation in electrically conducting fluids*. Cambridge, England, Cambridge University Press, 353 p., 1978.
- [68] H. Bondi, *On spherically symmetrical accretion*, *Mon. Not. R. Astron. Soc.* **112** (1952) 195–+.
- [69] W. H. McCrea, *Shock Waves in Steady Radial Motion Under Gravity.*, *Astrophys. J.* **124** (Sept., 1956) 461–+.
- [70] T. A. Ensslin, P. L. Biermann, P. P. Kronberg, and X. Wu, *Cosmic-Ray Protons and Magnetic Fields in Clusters of Galaxies and Their Cosmological Consequences*, *Astrophys. J.* **477** (Mar., 1997) 560–+, [[astro-ph/](#)].

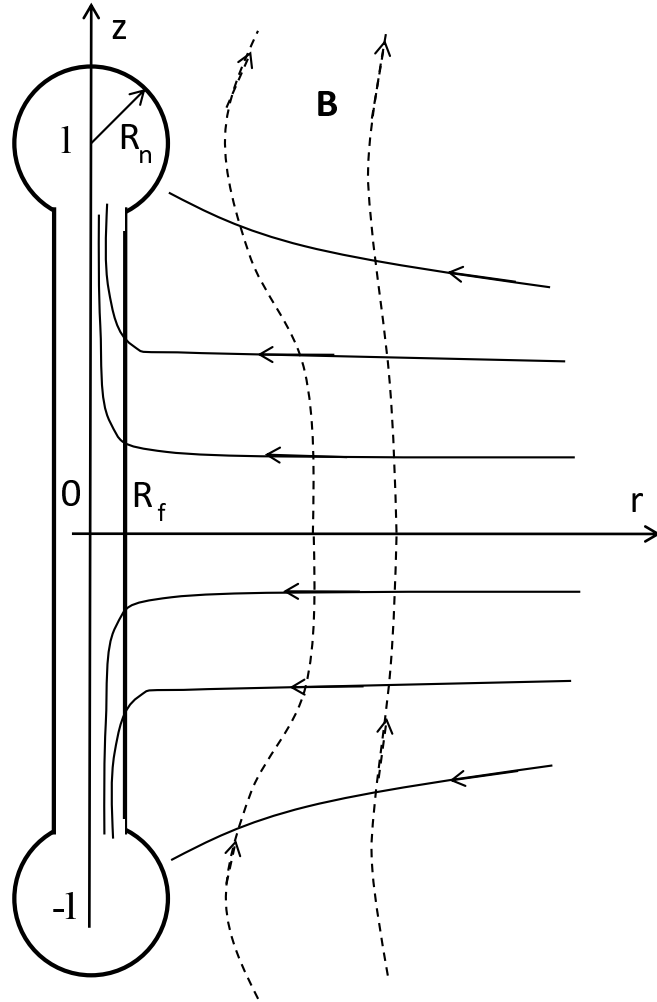


Figure 1. Sketch of the flow pattern (solid lines with arrows) and magnetic field geometry (dashed lines) near the 'dumbbell' structure consisting of one filament and two nodes at its ends.

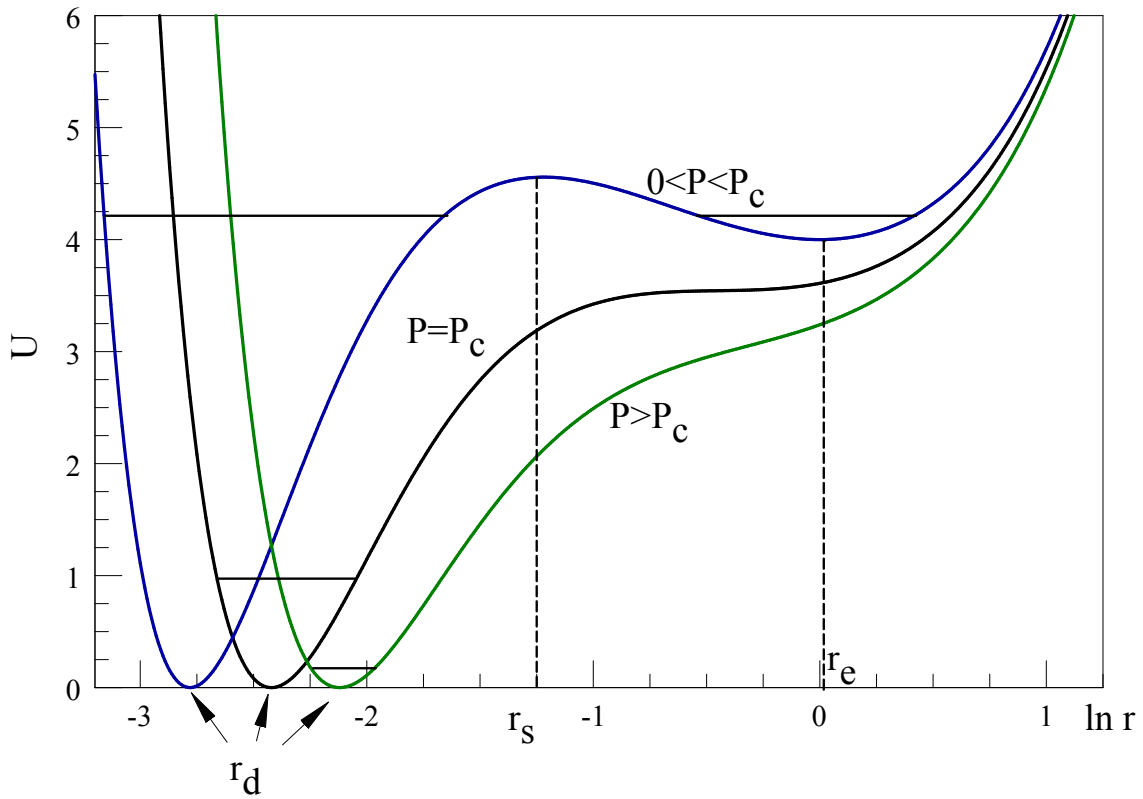


Figure 2. Potential energy of a particle as a function of r , as it evolves in time when $\mathcal{P}(t)$ varies from $\mathcal{P}(t) > \mathcal{P}_c$ to $\mathcal{P}(t) < \mathcal{P}_c$. Note that the radial direction is given in a logarithmic scale, for clarity. In reality, the potential well at smaller r is much narrower than that at larger r . The motion in the broad potential well corresponds to very large orbit radius, which is equivalent to particle escape from the accelerator.

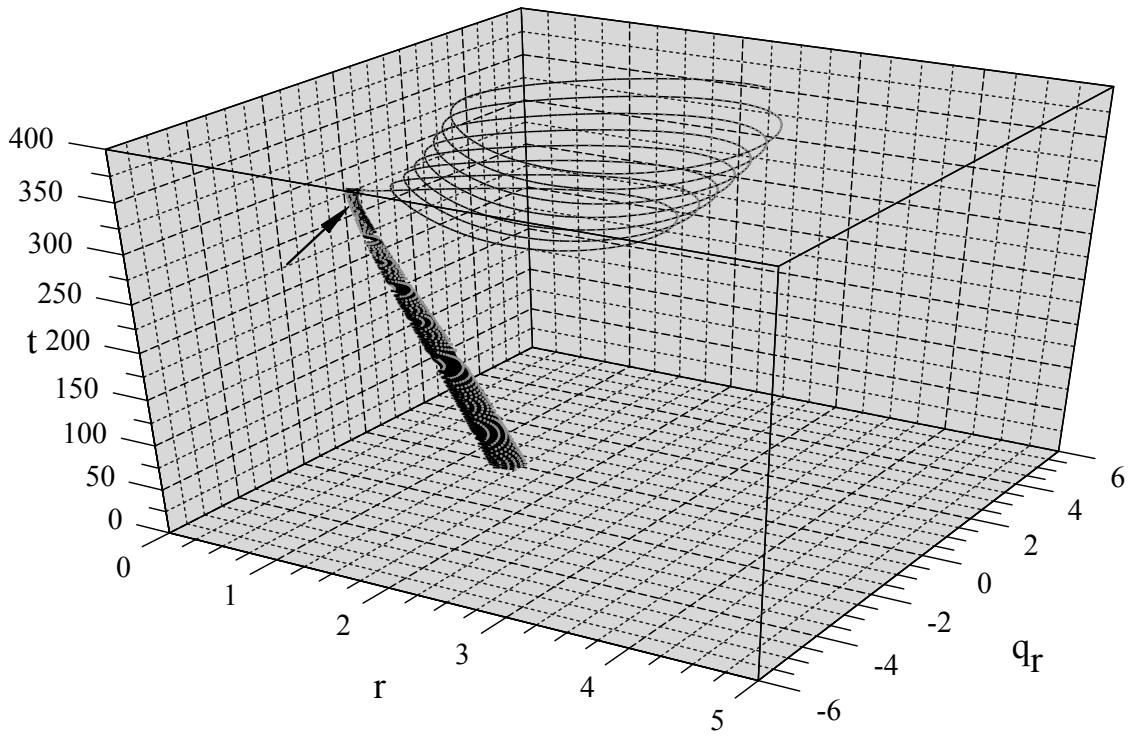


Figure 3. 3D particle trajectory with time pointing upward and with (r, q_r) horizontal phase plane coordinates, where $q_r = rp_r$. The particle starts its motion by drifting towards the filament from a distance $r = 1.5$, then it circulates around the filament (small r , also shown with arrow) and, finally, it crosses the separatrix (see Fig.4) and becomes detrapped from the filament. The particle remain bounded only by the ambient magnetic field (upper part of the trajectory)

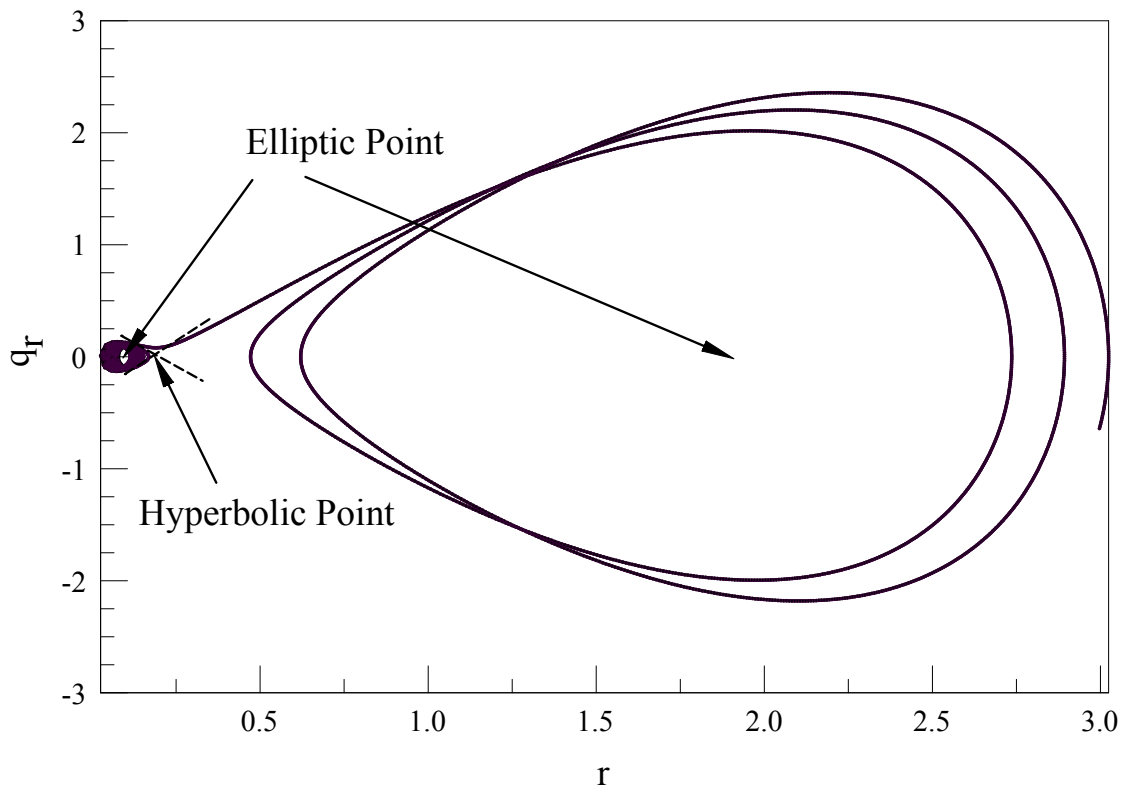


Figure 4. Two parts of particle trajectory (shown in Fig.3) after approaching the filament. The first part is to the left from a hyperbolic point (betatron regime). The second part is when particle crosses the separatrix and transitions to a weakly bounded state to the right from the hyperbolic fixed point. Short pieces of the separatrix passing through the hyperbolic point are shown with the dashed lines

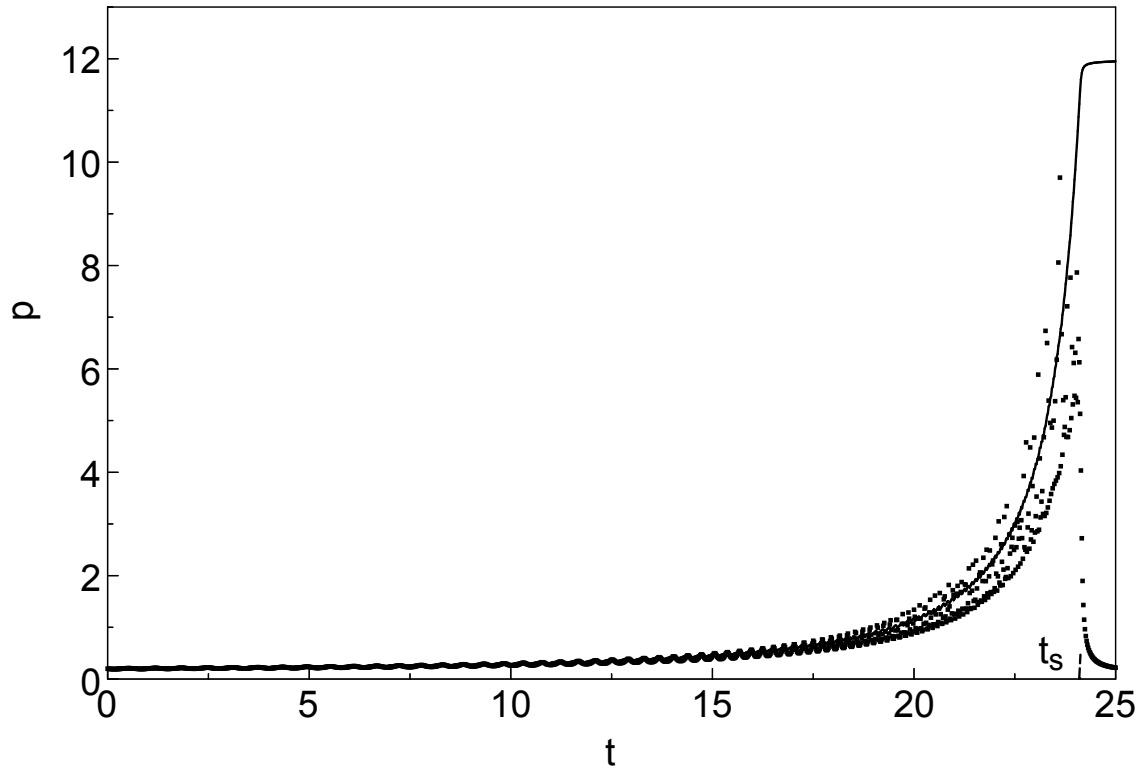


Figure 5. Acceleration of a particle with the initial momentum $p_0 = 0.2$ and coordinate $r_0 = 1$ ($B_0 = 2$), $v = 0.1$ (this case corresponds to the rightmost point on the plot shown in Fig.7). Solid line: numerical integration of the particle trajectory, shown as $p(t)$. Dots: $p(t)$ obtained from the condition $p^2/B(r) = \text{const}$ with $r(t)$ taken from the actual particle trajectory. Significant spreading of points illustrates the inaccuracy of the above representation of the adiabatic invariant near the separatrix.

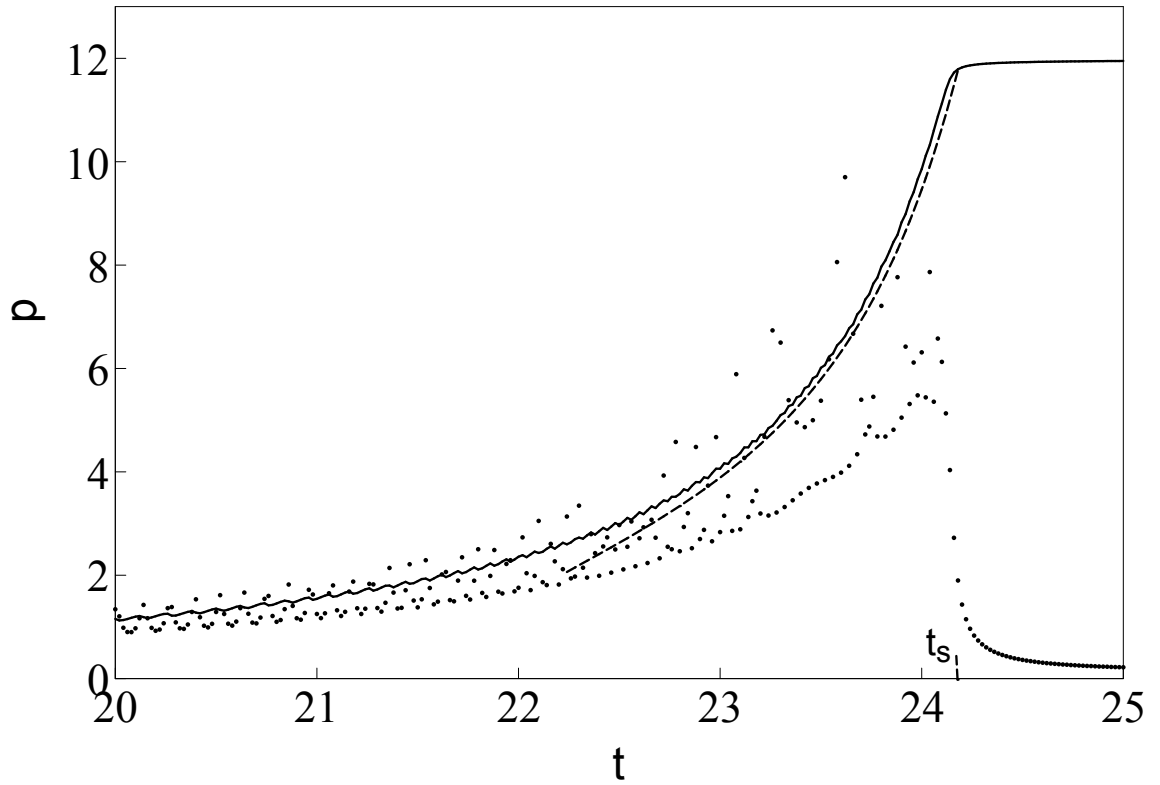


Figure 6. Final phase of the acceleration process, as shown in Fig.5. Numerical calculation of the particle trajectory is shown with the solid line, whereas the dots represent the same (adiabatic) $p(t)$ as in Fig.5. The approximate analytic solution, represented by eq.(B.6), is plotted with the dashed line.

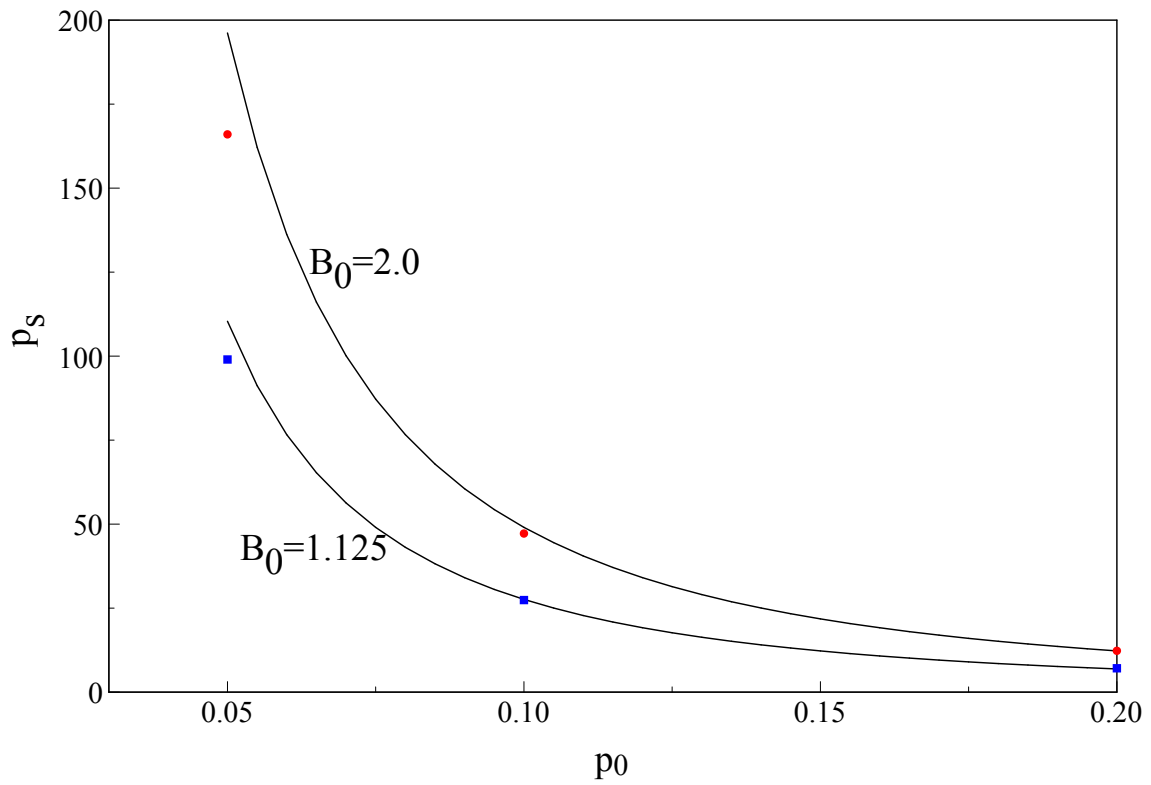


Figure 7. Particle maximum momentum p_s (at separatrix crossing) as a function of the initial momentum p_0 , plotted for two initial coordinates of the particle that correspond to the two indicated magnetic field values. Solid lines represent eq.(3.25), while the numerical solutions are shown by squares and circles.

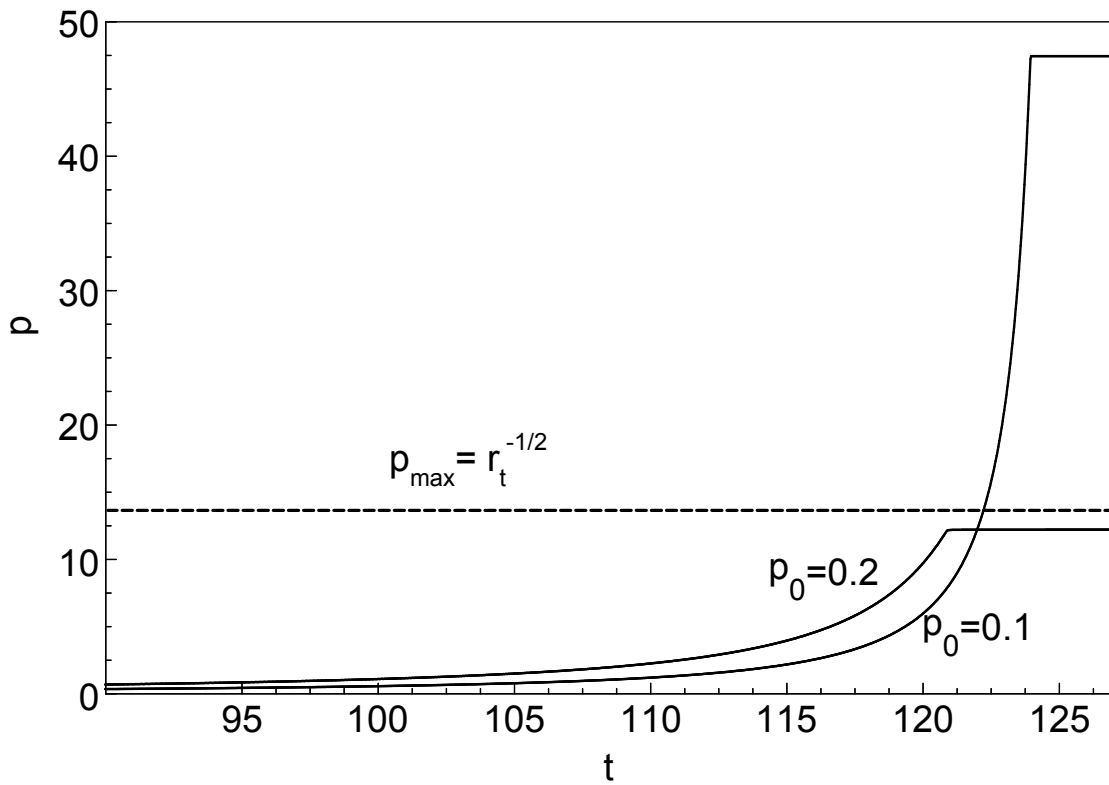


Figure 8. Example of two particle orbits with different initial momenta $p_0 = 0.1, 0.2$ (also shown as points in Fig.7). While the trajectory with the smaller initial momentum formally ends up at the larger final momentum, changing the flow direction towards one of the nodes (this happens at $r = r_t \sim 10^{-2}$, which is marked by the dashed horizontal line) prevents the particle with the higher final energy from escaping the filament.

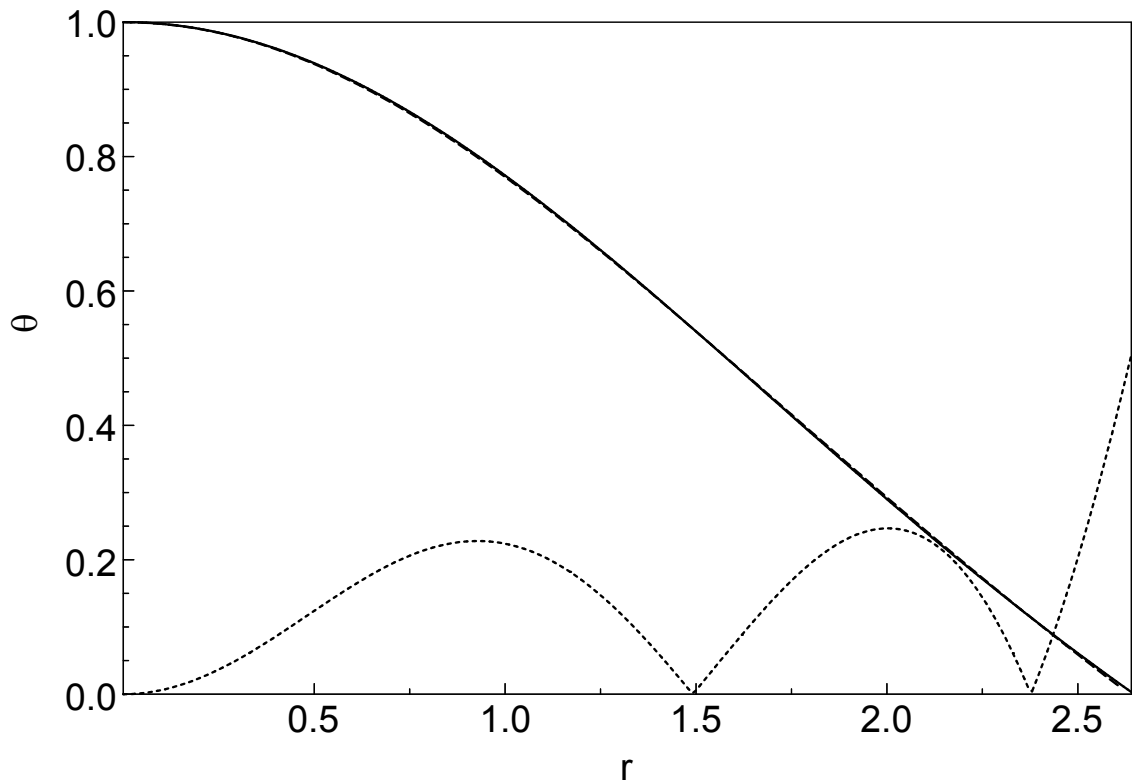


Figure 9. Numerical solution of eq.(A.4) ($d = 2$, cylindrical symmetry) and its Padé approximation, plotted as the solid and the dashed line, respectively. As the difference is barely visible, the absolute value of it multiplied by 100 is shown with the dotted line. The solution for $d = 3$ is similar, and therefore not shown here.

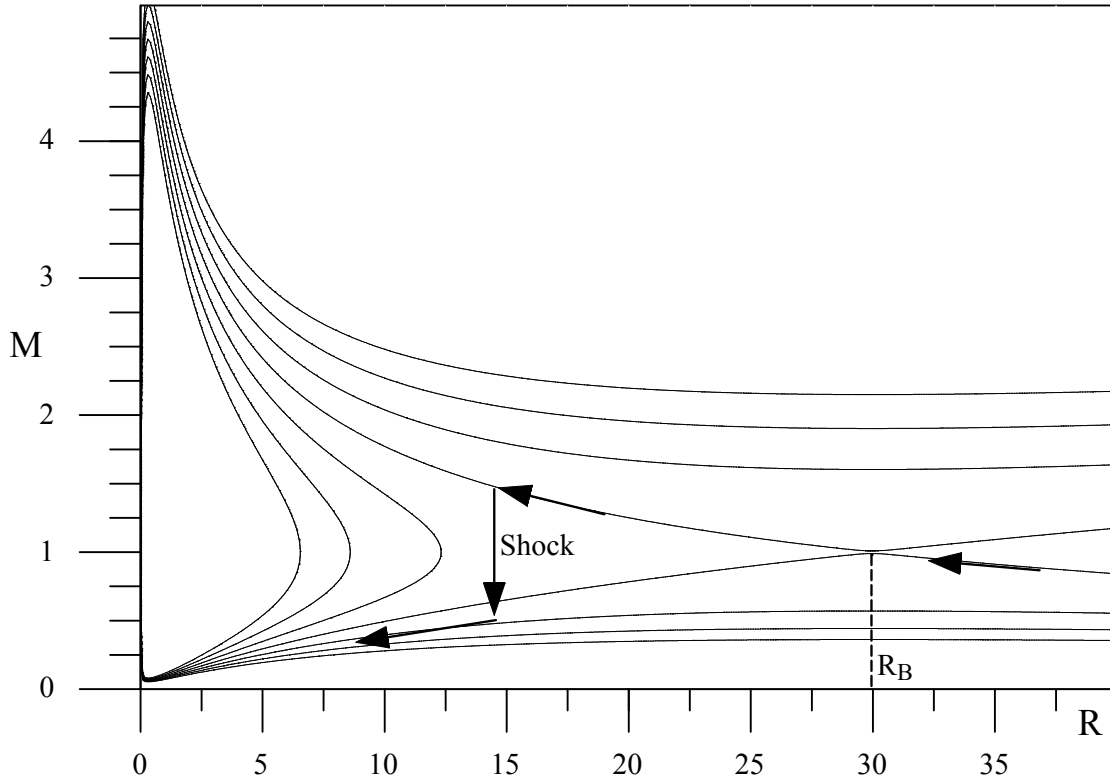


Figure 10. Bondi diagram for a radial accretion flow onto a filament shown in distance $R = r/l$ - Mach number \mathcal{M} variables. A gas envelope (arrows) passes through a sonic point at $\mathcal{M} = 1$, $R = R_B$. Then, after being accelerated and shocked, it jumps to a lower branch (vertical arrow) of the flow diagram, decelerates further and becomes strongly compressed before turning towards one of the nodes, shown in Fig.1.